

AD\_\_\_\_\_

Award Number: W81XWH-07-1-0188

TITLE: Development and Application of Advanced Ophthalmic Imaging Technology to Enhance Military Ocular Health Capabilities

PRINCIPAL INVESTIGATOR: Shuliang Jiao, Ph.D.

CONTRACTING ORGANIZATION: University of Miami  
Coral Gables 33124

REPORT DATE: April 2008

TYPE OF REPORT: Annual

PREPARED FOR: U.S. Army Medical Research and Materiel Command  
Fort Detrick, Maryland 21702-5012

DISTRIBUTION STATEMENT: Approved for Public Release;  
Distribution Unlimited

The views, opinions and/or findings contained in this report are those of the author(s) and should not be construed as an official Department of the Army position, policy or decision unless so designated by other documentation.

<b>REPORT DOCUMENTATION PAGE</b>				Form Approved OMB No. 0704-0188	
Public reporting burden for this collection of information is estimated to average 1 hour per response, including the time for reviewing instructions, searching existing data sources, gathering and maintaining the data needed, and completing and reviewing this collection of information. Send comments regarding this burden estimate or any other aspect of this collection of information, including suggestions for reducing this burden to Department of Defense, Washington Headquarters Services, Directorate for Information Operations and Reports (0704-0188), 1215 Jefferson Davis Highway, Suite 1204, Arlington, VA 22202-4302. Respondents should be aware that notwithstanding any other provision of law, no person shall be subject to any penalty for failing to comply with a collection of information if it does not display a currently valid OMB control number. <b>PLEASE DO NOT RETURN YOUR FORM TO THE ABOVE ADDRESS.</b>					
1. REPORT DATE (DD-MM-YYYY) 01-04-2008		2. REPORT TYPE Annual		3. DATES COVERED (From - To) 06 MAR 2007 - 05 MAR 2008	
4. TITLE AND SUBTITLE  Development and Application of Advanced Ophthalmic Imaging Technology to Enhance Military Ocular Health Capabilities				5a. CONTRACT NUMBER	
				5b. GRANT NUMBER W81XWH-07-1-0188	
				5c. PROGRAM ELEMENT NUMBER	
6. AUTHOR(S) Shuliang Jiao, Ph.D.  E-Mail: sjiao@med.miami.edu				5d. PROJECT NUMBER	
				5e. TASK NUMBER	
				5f. WORK UNIT NUMBER	
7. PERFORMING ORGANIZATION NAME(S) AND ADDRESS(ES)  University of Miami Coral Gables 33124				8. PERFORMING ORGANIZATION REPORT NUMBER	
9. SPONSORING / MONITORING AGENCY NAME(S) AND ADDRESS(ES) U.S. Army Medical Research and Materiel Command Fort Detrick, Maryland 21702-5012				10. SPONSOR/MONITOR'S ACRONYM(S)	
				11. SPONSOR/MONITOR'S REPORT NUMBER(S)	
12. DISTRIBUTION / AVAILABILITY STATEMENT Approved for Public Release; Distribution Unlimited					
13. SUPPLEMENTARY NOTES					
14. ABSTRACT The goal of this research is to advance the frontiers of a promising imaging technology called optical coherence tomography (OCT), developing advanced instrumentation and new software applications to enable high resolution evaluations of the retina and optic nerve that could be easily performed by non-physician health care professionals. The research achieved the following aims: 1) Developed methods for accurate vertical alignment and matching, including the overlay of a color or red-free, fundus photograph on an OCT image for registration; 2) Developed the mathematical algorithms to analyze and quantify OCT datasets automatically including 3D segmentation algorithm for quantitative mapping of the retinal thickness using 3D OCT data for normal and diseased human eyes; 3) Further improved the resolution of the spectral OCT. The developed OCT system has a depth resolution of ~3 µm in tissue and is capable of resolving all the sub-retinal features of the retina. The system is also capable of delineate the anatomical structure of the cornea with high imaging quality. The system provides a good diagnostic tool for diseases of both the anterior and posterior segments of the eye.					
15. SUBJECT TERMS Optical coherence tomography, image segmentation, image registration					
16. SECURITY CLASSIFICATION OF:			17. LIMITATION OF ABSTRACT	18. NUMBER OF PAGES	19a. NAME OF RESPONSIBLE PERSON
a. REPORT	b. ABSTRACT	c. THIS PAGE			USAMRMC
U	U	U	UU	40	19b. TELEPHONE NUMBER (include area code)

## TABLE OF CONTENTS

	Page
Introduction.....	4
BODy .....	4
Key Research accomplishments .....	24
Reportable outcomes.....	24
Conclusion .....	25
References.....	25
APPENDICES .....	27

# INTRODUCTION

Millions of Americans, including a large percentage of active military personnel and veterans, are affected by three major blinding diseases of the retina and optic nerve: diabetic retinopathy, age-related macular degeneration, and glaucoma. These diseases typically affect the elderly, but a significant number of young people also fall victim. As a result of current advances in surgical and pharmacologic therapeutics, vision loss due to all these diseases can be halted or even reversed if the disease is detected early. New advanced detection methods are available, but are only interpretable by very experienced specialists. The goal of this research is to advance the frontiers of a promising imaging technology called optical coherence tomography (OCT), developing advanced instrumentation and new software applications to enable high resolution evaluations of the retina and optic nerve that could be easily performed by non-physician health care professionals. In addition to on-site use, such techniques could be further applied for telemedicine transmittal of images (from the battlefield or other remote sites) for further evaluation by specialist ophthalmologists. The hypothesis to be tested is that advancements in OCT technology will enhance military and nonmilitary ocular health capabilities. The three specific research objectives are as follows: 1) Develop methods for accurate vertical alignment and matching, including the overlay of a color or red-free, fundus photograph on an OCT image for registration. 2) Develop the mathematical algorithms to analyze and quantify OCT datasets automatically. 3) Further improve the resolution of the spectral OCT, correlate images with pathology, and develop algorithms for 3-D visualization of datasets.

## BODY

### **Task 1. Development of algorithms for quantitative evaluation of retinal pathology and for monitoring disease progression and response to treatment.**

a. *Develop 3D segmentation algorithm for quantitative mapping of the retinal thickness using current 3D OCT data for normal and diseased human eyes.*

The development of high-speed spectral-domain OCT systems allows for the introduction of new imaging modalities, including the acquisition of three-dimensional datasets. Detailed information about the retinal structure over large areas is encoded in these 3-D datasets. A crucial challenge to exploiting the full potential of retinal OCT imaging is the ability of extracting reliable, quantitative information from the scans. Our efforts towards providing an answer to this question are an important component of the research supported by the grant. In particular we developed, implemented and validated 3D segmentation algorithms to map the retinal geometry from the OCT datasets. One of the main products of the segmentation is the measurement of retinal thickness. Such measurements provide the framework for the quantitative evaluation of retinal pathology. Multimodal registration between OCT fundus reconstructions and other en face retinal images (i.e. fundus photography, fluorescein angiography, fundus autofluorescence) gives us the tools to map the precise retinal site corresponding to each image pixel and track a specific location over time (across successive datasets). This provides an unprecedented ability for monitoring disease progression and response to treatment. This type of information could prove very valuable to the physician in formulating clinical decision as well as for improving the understanding of pathological processes.

The first step involved developing image processing software to perform tasks such as feature recognition and edge segmentation. There are several issues that make segmentation of OCT images very difficult in general. Some of the main complications that one needs to overcome are the presence of speckle noise, the relative low contrast and signal to noise ratio in a OCT image compared to x-ray CT and MRI imaging, and the large variability of retinal features' appearance, especially in the presence of pathology. The difficulty in extracting quantitative information from OCT images is well illustrated by the problems with the commercial OCT instrument (StratusOCT, Carl Zeiss), whose retinal thickness analysis has been shown to generate a large number of artifacts. An additional problem in 3D spectral-domain OCT imaging is the very big size of the datasets. The very large number of A-scans to be analyzed (>40000) greatly restricts the acceptable rate of failure of the algorithms to be used, before errors become clearly evident. Also the computational power/time needs of potential algorithms need to be taken into careful consideration.



The algorithms developed by our group allow us to reconstruct the three dimensional geometry of the patient's retina. In particular we can visualize the geometry of the internal limiting membrane (ILM) and the retinal pigment epithelium (RPE) as surfaces in a three dimensional space. In Fig. 1, we show this construct for the retina of a patient suffering from non-exudative age-related macular degeneration (AMD). Retinal thickness maps, i.e. the distances between ILM and RPE, can be then computed and visualized. The retinal thickness maps we can generate from SD-OCT images are vastly more detailed, accurate, and reproducible than those available with StratusOCT or any other current imaging technology.

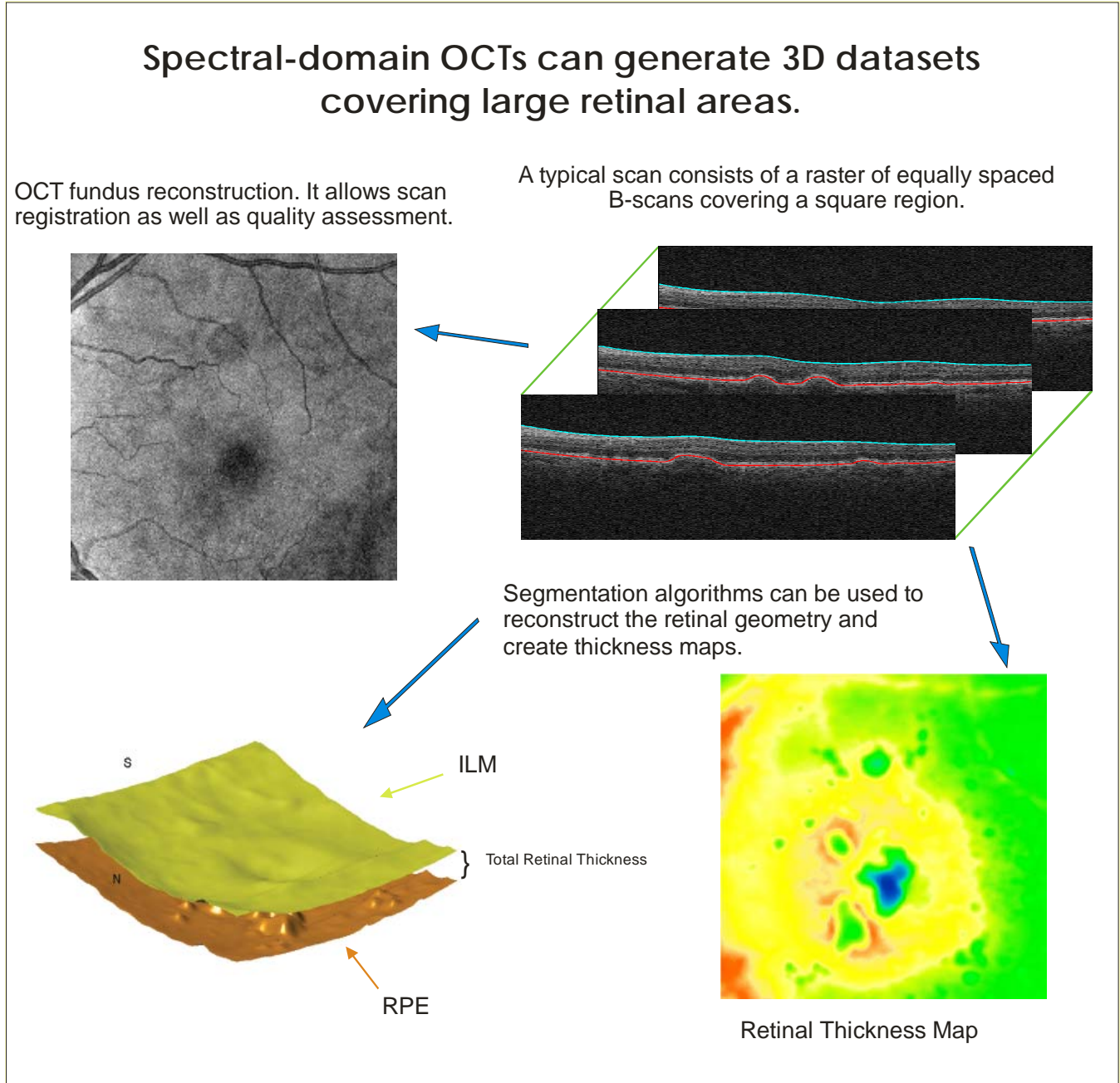


Fig. 1 Our analysis of OCT datasets.

The algorithms we developed are based on an iterative architecture, where an initial guess is successively evaluated and improved upon, according to a set of principles that may be tailored to the specific structure to be analyzed and/or the particulars of the disease model of interest. The general design of the algorithms is described in the following flowchart (Fig. 2).

We will assume here that we are dealing with an OCT dataset acquired using a raster scan consisting of  $d_A \times d_H \times d_V$  data points, where  $d_A$  is the A-scan size,  $d_H$  is the number of scans in each B-scans, and  $d_V$  is the number of B-scans in the raster scan. The OCT dataset is then a  $d_A \times d_H \times d_V$  dimensional array  $A(i,j,k)$ , where the pixel

indexes are equivalent to a system of 3-dimensional Euclidean orthogonal coordinates. The main output consists of two  $d_H \times d_V$  arrays representing the ILM and the RPE positions, i.e. the ILM(j,k) entry is an integer giving the pixel number in the A-scan  $A(.,j,k)$  corresponding to the ILM leading edge.

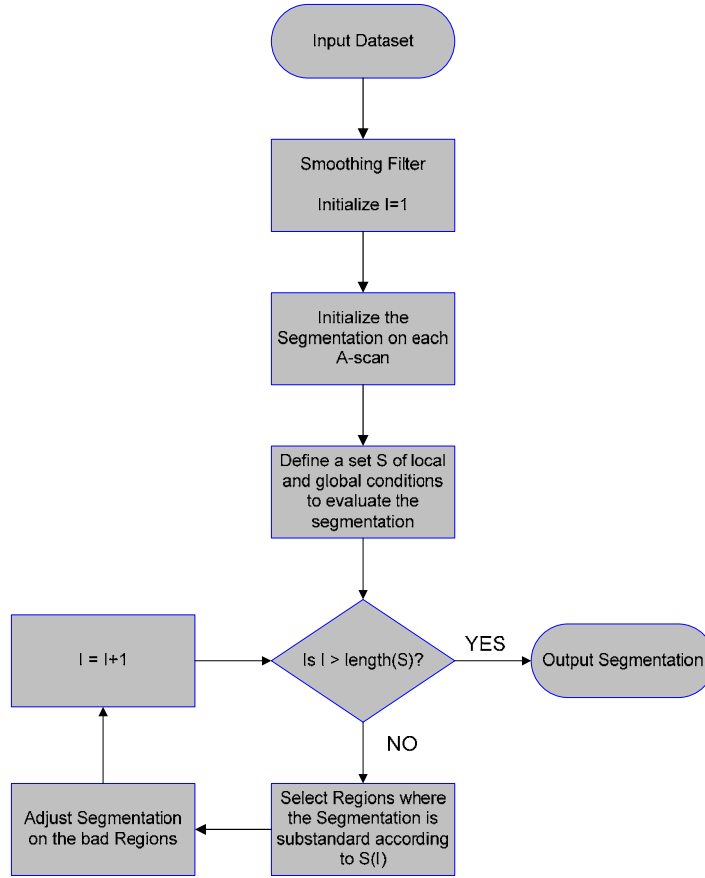


Fig. 2. Basic Structure of the Algorithm.

The first step consists of some preprocessing the OCT data, whose main purpose is to reduce the amount of speckle noise and then computing some basic statistical characteristics of the remaining noise process. Also some signal-level normalization is achieved.

At this point a quick analysis of each A-scan is carried out to produce an initial estimate for the ILM and RPE arrays. While it would of course be desirable to achieve the correct segmentation already at this stage, our approach only requires that this initial estimate be “mostly correct”. This is actually the main assumption behind the design of the algorithm: if at least a sizable percentage on the boundaries can be quickly estimated in a correct manner (and if we can recognize this correct region), then we can focus our computational resources effectively on the “bad regions” to improve the result.

An iteration loop is therefore set up where the algorithm repeatedly improves the segmentation results by selecting “bad regions” where the current segmentation is “suspect” and analyzing these bad regions more carefully. The process stops when either there are no bad regions left or the algorithm has traversed a preset maximal number of loops. The routines which decompose a given segmentation in good and bad regions, and the routines that analyze and correct the segmentation on the bad regions, are the computational core of the algorithm. They strive to encode a series of hypotheses as well as a fair amount of empirical knowledge on the anatomy and geometry of the retina. The concentration of this knowledge into a suitable set of mathematical conditions which do a good job of discriminating problematic areas in the segmentation, and work well across a

very wide spectrum of retinal conditions, is the crucial task to be achieved. We believe our choices can be shown to perform quite successfully.

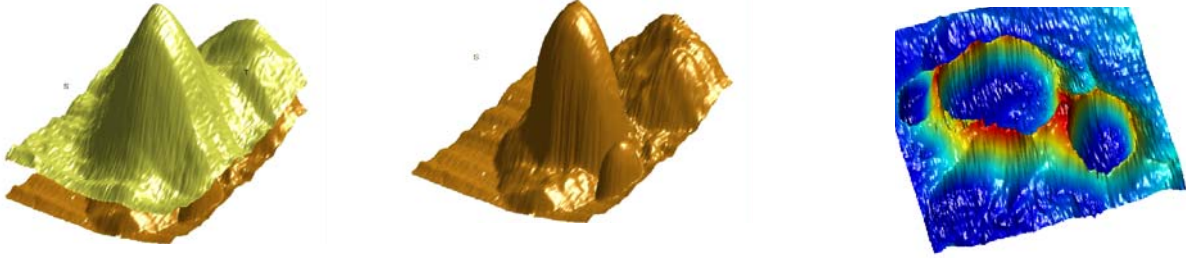


Fig. 3. Segmentation result for a human retina with RPE detachment. **Left:** 3D view of the segmented ILM and RPE; **Center:** 3D view of the segmented RPE; **Right:** the calculated retinal thickness map.

We have focused so far on tools that describe the ILM and the RPE, i.e. the inner and outer boundaries of the retina. However, these algorithms could be generalized to provide quantitative information about the damage to different biological layers caused by the diseases, like for instance the nerve fiber layer (NFL), the ganglion cell layer (GCL), or the photoreceptors. The ability to accurately measure such retinal structures would likely further our understanding of the progression of various retinal diseases.

*b. Develop 3D registration algorithm for monitoring disease progression and response to treatment using current 3D OCT data.*

Multimodal and intra-modal retinal image registration is important to clinical diagnosis and treatment. Currently, there are several types of retinal imaging modalities, including OCT, fluorescein angiogram, fundus autofluorescence imaging, and color fundus photography. Different types of imaging reveal different characteristics the retina by using different contrast mechanisms, which provide complimentary localized information of the retina. At the same time, retinal images taken at different time can reveal the progression and the response to treatment of retinal diseases. We have developed an effective algorithm to register the various types of fundus images: OCT fundus images taken at different times and OCT fundus images to color fundus photograph of the same eye.

Registration methods usually consist of several steps [1-3]: feature detection; transform model estimation; optimization function design; and optimization strategies. We do not choose intensity-based feature for multimodal image registration because even for intra-modal retinal images, intensity can change due to changes in imaging parameters. For retinal image registration, blood vessel patterns [4,5] can be taken as a relatively stable feature. Some papers use the vascular landmarks [6,7], like bifurcations and crossovers [8]. However, for low quality images or images with disease, it is not easy to detect bifurcations and crossovers.

Here, we use blood vessel ridges as a specific feature [9]. Defined as points where the image has an extremum in the direction of the largest surface curvature [10], ridges are a natural feature of blood vessels and are usually approximately center lines of blood vessels. By using ridges we can avoid the problem of determining the whole blood vessel area, which not only saves computation time but also avoids the potential bad effect of imprecisely detected vessel area on registration.

Among different transformation models, like translation, affine, and quadratic models [5, 6], affine transformation is relatively simple while generating acceptable results:

$$(x' \ y' \ 1) = (x \ y \ 1) \begin{pmatrix} a_{11} & a_{12} & 0 \\ a_{21} & a_{22} & 0 \\ a_{31} & a_{32} & 1 \end{pmatrix} \quad (1)$$

where, the point  $(x, y)$  in one image will be transformed to  $(x', y')$  in the other image by the affine

transformation matrix  $\begin{pmatrix} a_{11} & a_{12} & 0 \\ a_{21} & a_{22} & 0 \\ a_{31} & a_{32} & 1 \end{pmatrix}$ , which includes the combination of translation, rotation, shearing and

scaling. In the transformation matrix,  $a_{31}$  and  $a_{32}$  are translation parameters,  $a_{11}$ ,  $a_{12}$ ,  $a_{21}$ , and  $a_{22}$  are parameters related to shear, rotation and scale. We use the affine transformation model in our retinal image registration algorithm.

Optimization function is to evaluate the similarity between a pair of images. For intensity based matching [1], correlation, mutual information, and Fourier transformation can be used as an optimization function. For registration with points as features [7, 5], distance is a good similarity measurement. In literature there are a lot of similarity functions [11-13] to compute distance between points.

After the optimization function is chosen, we need to choose a proper optimization strategy [2]. Here, we focus on optimization strategies using points as features, since our algorithm uses vessel ridges as features. Ref. 6 used a hierarchy of models, a random sampling search technique and iteratively-reweighted least-squares to estimate the quadratic transformation. A dual-bootstrap iterative closest point algorithm is used in Ref. 7. Usually initialization does not yield points suitable for global optimization except for some local area, so it is not necessary to match all the points. Since the alignment in the small initial region is reasonably accurate, it helps to expand registration area gradually. Ref. 5 used brute force search to get translation estimation, then estimated the affine or quadratic transformations by iterative closes point algorithm. The test fundus images are at a similar scale.

Our algorithm adopts vessel ridges as features. For different fundus images, they have different resolutions. According to the resolution parameters, we rescale fundus vessel ridge images to a similar scale. Brute force search is first used to estimate the translation parameters and scale parameter. Then the translation and scale estimation with the largest similarity is taken as the initialization of the iterative closes point algorithm (ICP) to get a more accurate transform. Experiments show that affine transform works well.

Three steps were taken in the registration algorithm:

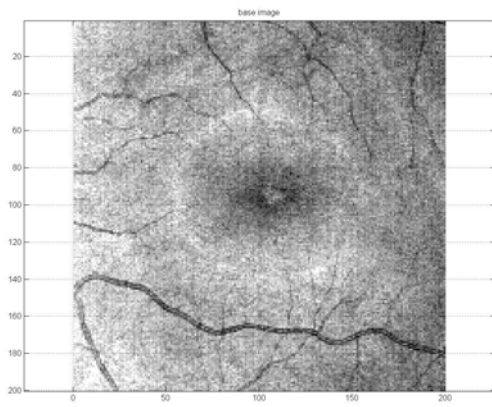
Step 1: Vessel ridges are detected for different fundus images.

Step 2: Brute force search is used to estimate the translation parameters and scale parameter. For different types of fundus images, rescale parameter and the size of the matching area are estimated as input parameters.

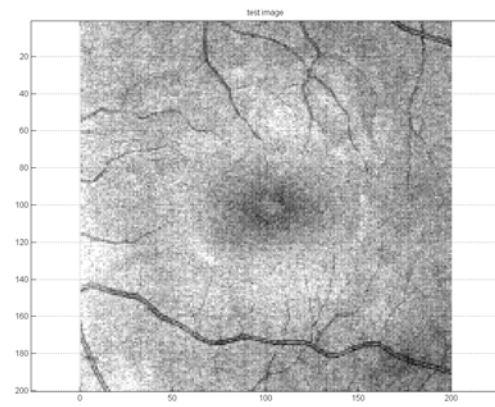
Step 3: With the estimation of translation and scale parameters, the iterative closest point algorithm (ICP) is used to find a more exact affine transform.

Fig. 4 test registration result for OCT fundus image vs OCT fundus image. The images were taken separately in the same day for a patient. (a) base image. (b) test image. (c) the registration of detected blood vessel ridges for the two images. (d) registered test image.

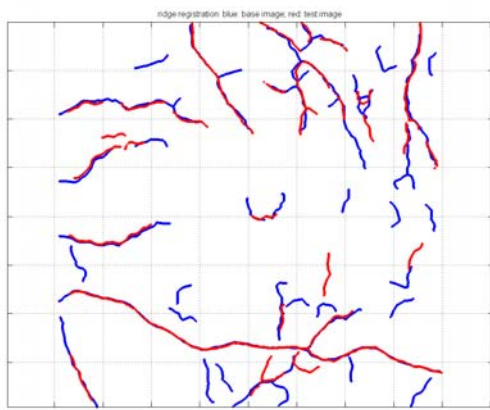
shows the registration result for an OCT fundus image vs. OCT fundus image. The OCT images were acquired with Carl Zeiss' Cirrus separately in the same day. Fig. 5 shows the test result for another patient imaged at different dates. Fig. 6 shows the comparison of registration algorithms based on intensity with that based on blood vessel ridges. We can see that the feature of vessel ridges is more stable than that of intensity. We used ImageJ software in Ref. 14 to register the two examples for comparison because our registration algorithm can not be applied to intensity based registration. Fig. 7 shows the test result fro registration of the OCT fundus image on the color fundus photo.



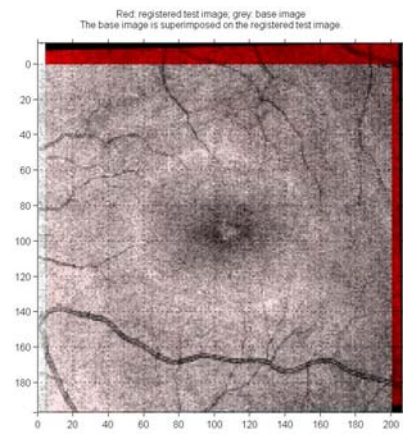
(a) Base image



(b) Test image



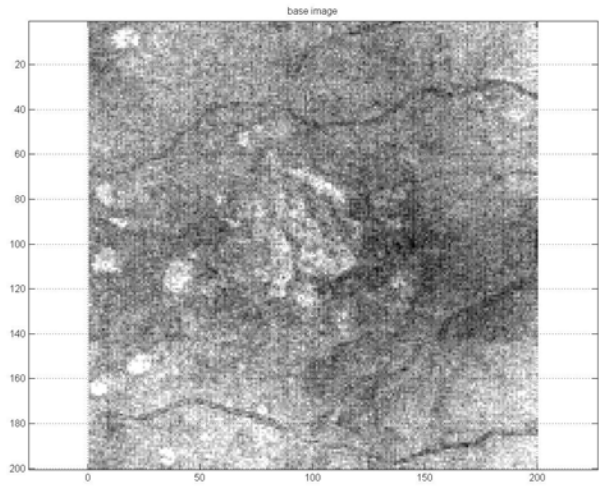
(c) The registration of detected blood vessel ridges for the two images.



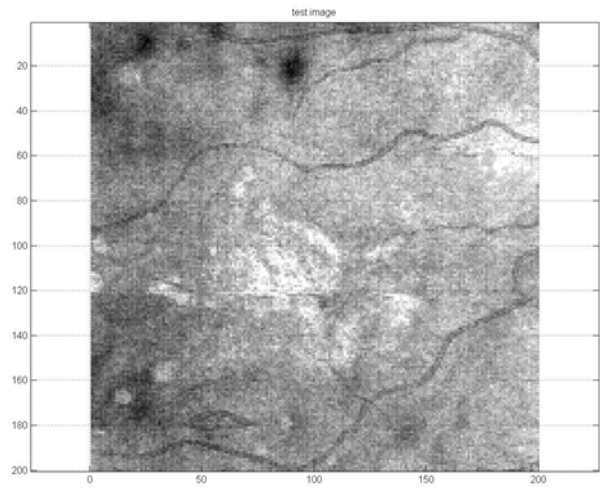
(d) Registration result.

Fig. 4 test registration result for OCT fundus image vs OCT fundus image. The images were taken separately in the same day for a patient. a) base image. (b) test image. (c) the registration of detected blood vessel ridges for the two images. (d) registered test image.

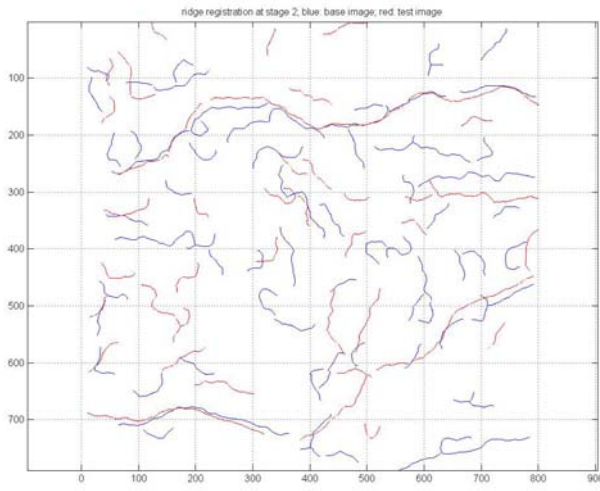




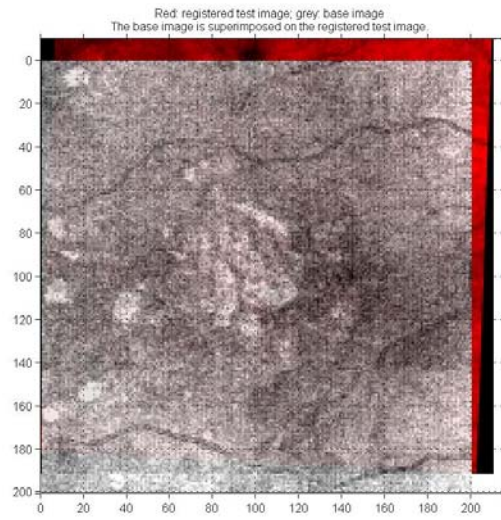
(a) Base image



(b) Test image

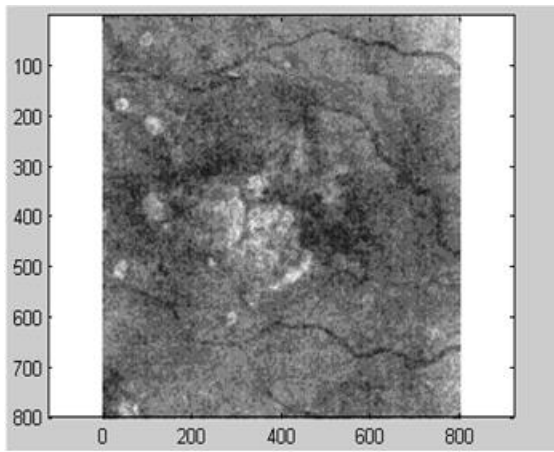


(c) The registration of detected blood vessel ridges for the two images.

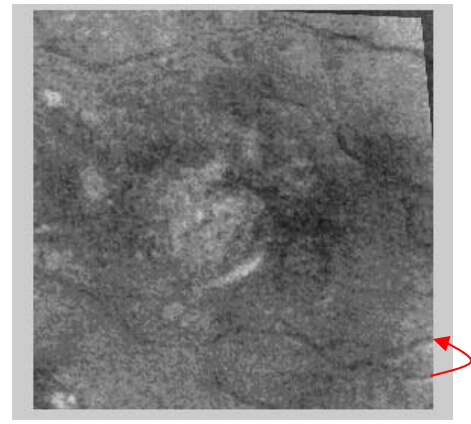


(d) Registration result.

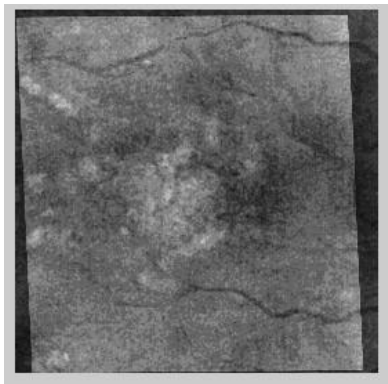
Fig. 5 test registration result for OCT fundus image vs OCT fundus image. The images were taken at different dates.



(a) Base image

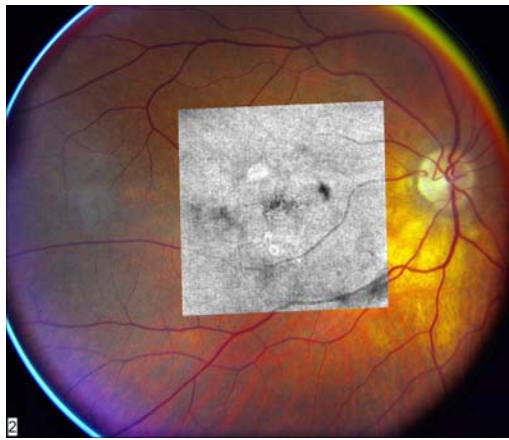


(b) The base image is under the registered test image based on intensity by ImageJ software. We can see clearly the deviation of corresponding vessels.



(c) The base image is under the registered test image based on vessel ridges by ImageJ software.

Fig. 6 Comparison of registration algorithms based on intensity with that based on blood vessel ridges. We can see that the feature of vessel ridges is more stable than that of intensity. We used ImageJ software in Ref. 14 to register the two examples for comparison because our registration algorithm can not be applied to intensity based registration.



(a) The registration result. The OCT fundus image is superimposed on the color fundus image.



(b) The registration of detected blood vessel ridges for the two images.

Fig. 7 test registration result for OCT fundus image vs color fundus photo.

c. Test the accuracy of the segmentation algorithm by comparing the segmentation results done by the algorithm and by experts, respectively.

The performance of a segmentation algorithm like the one described here can be judged in terms of two important measures: accuracy and reproducibility. These characteristics are not necessarily related and are both important for clinical applications. Also algorithms' performance should be evaluated on the full range of pathologies presented in the patient population. The accuracy of any new algorithm has to be tested by comparing the retinal boundaries generated by the algorithm with boundaries manually generated by an expert, e.g. a clinician or a pathologist who is familiar with OCT image interpretation. This information can be used to evaluate the performance of the algorithms, as well as to quantify further improvements. Testing the reproducibility involves scanning a given set of eyes repeatedly. Because it is often difficult to image exactly the same retinal area every time, the ability to perform image registration becomes an important component of assessing the reproducibility of measurements in the context of spectral domain OCT.

For the analysis of the segmentation algorithm's performance we focused on raster scans covering a 6x6x2 mm volume and acquiring either 200x200 A-scans equally spaced on the retina or 512x128 A-scans covering the same region. Automated segmentation of the internal limiting membrane (ILM) and anterior retinal pigment epithelium (RPE) boundaries generates surfaces in 3-D space and retinal thickness maps.

132 eyes from patients imaged at Bascom Palmer were randomly selected representing the full range of retinal diseases. Also included were 12 eyes of normal volunteers. For each eye a SD-OCT dataset was entered in the study. The OCT datasets were divided amongst three retina specialist, who traced manually the ILM and RPE boundaries a number of predetermined B-scans. These manually drawn boundaries were then compared pointwise with the results of the automated segmentation.

The statistical distributions of the differences (pixelwise) between the manual and automated segmentations are described separately for ILM and RPE, for both normal eyes and eyes with disease. In addition to these error probability distributions, we defined a threshold for registration failure. A computer generated boundary was considered a failure if its distance from the corresponding "true edge" was above 20 pixels at least 10% of the time. Of course any such failure criteria are somewhat arbitrary, nevertheless we believe it come close to



capturing a clinical judgment about the usefulness/appropriateness of a given segmentation result. Two particular examples of algorithm failure are shown in Fig. 8.

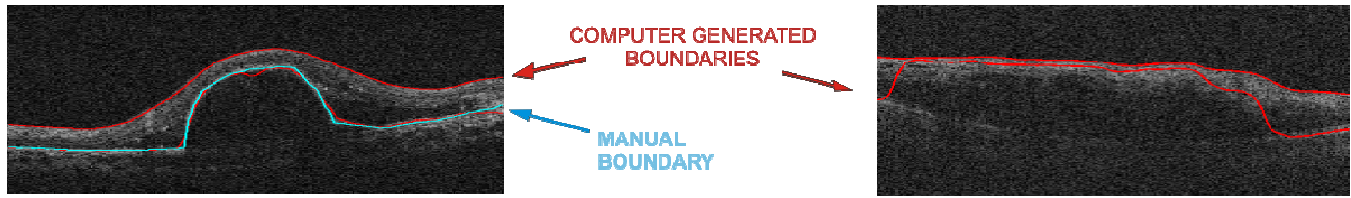


Fig. 8 Two B-scans showing failures of the RPE segmentation. Failures can be fairly subtle (example on the left) in the example on the right, or sometime substantial.

Normal subjects are of course the simplest case. The anatomical concepts are very clear, image quality tends to be good, and segmentation in this case is relatively easy. The segmentation algorithm did not fail on a set of 36 B-scans from 12 eyes. The difference probability distributions, shown below in Fig. 9, are very tight with means close to zero. The standard deviation is somewhat higher for the RPE than for the ILM, reflecting the fact that identifying the ILM boundary is in general a more straightforward task.

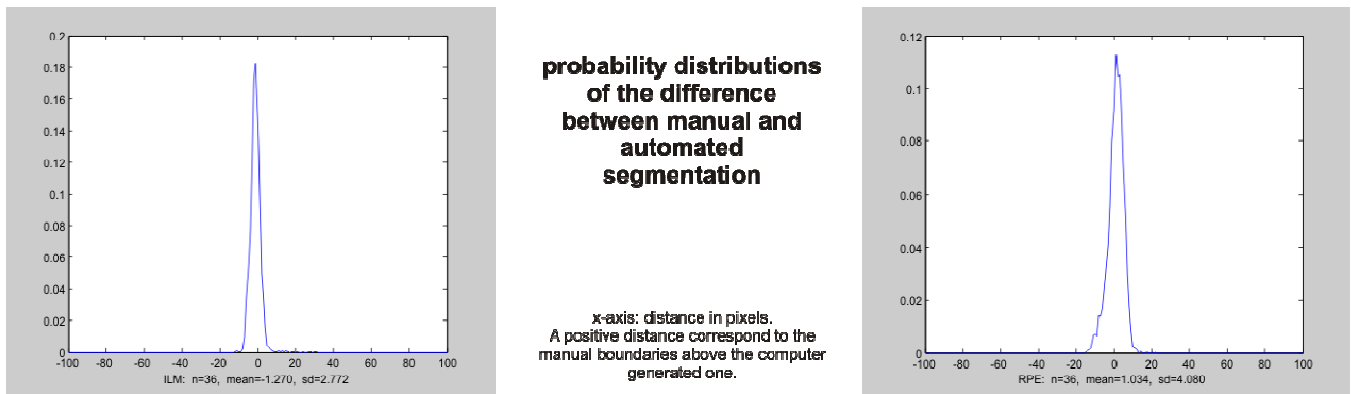


Fig. 9 Accuracy results for normal eyes.

Our sample of patients' eyes is meant to be representative of what is typically imaged at the Bascom Palmer retinal clinic. These are randomly chosen eyes presenting a full range of pathologies. No special provision was made to eliminate scans with less than optimal image quality. The idea was to obtain results which would evaluate the performance of the algorithm in a setting similar to what clinicians would actually see in a busy tertiary care center. While the presence of pathology clearly affects the performance of automated segmentation, the probability distributions remained quite narrow in all cases.

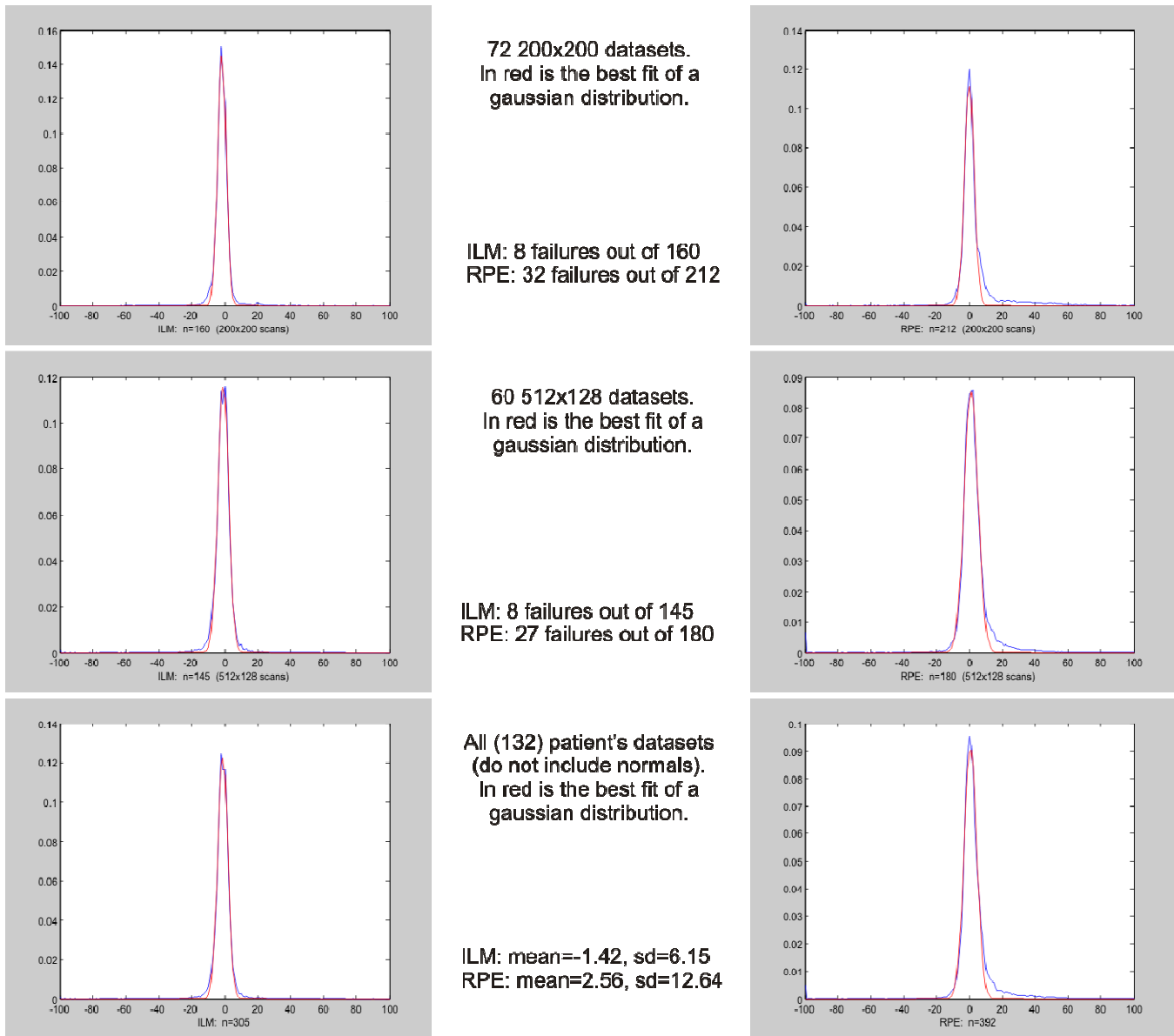


Fig. 10 Accuracy results for eyes with disease.

The variance of distribution of differences is larger by a factor roughly equal to three. The segmentation of the RPE shows a tendency to be slightly biased towards positive errors (i.e. the automated segmentation is more often below the manually drawn curve). On both scan patterns the ILM segmentation failed on  $\sim 5\%$  of the B-scans, while the RPE failed on  $\sim 15\%$  of the B-scans. It is important to keep in mind that it is often difficult to identify retinal structures (in particular the “RPE”) in the presence of pathologies (as a matter of fact it is often misleading to even use the word RPE to describe what is really an outer retinal edge. In many cases the actual RPE can be compromised and/or missing). Even the retinal experts could not sometime agree to a “right” position for the outer retinal edge. Therefore the results shown in Fig. 10 are quite encouraging.

The reproducibility of the retinal thickness measurements is estimated by computing the standard deviation, both pointwise and averaged over regions, of registered thickness maps. Variations in OCT measurements are in general due to several factors. Datasets acquired with the new SD-OCT instruments can in principle be registered using the OCT fundus images, therefore minimizing the component of variation due to eye movements as well as scan aiming/patient fixation problems.

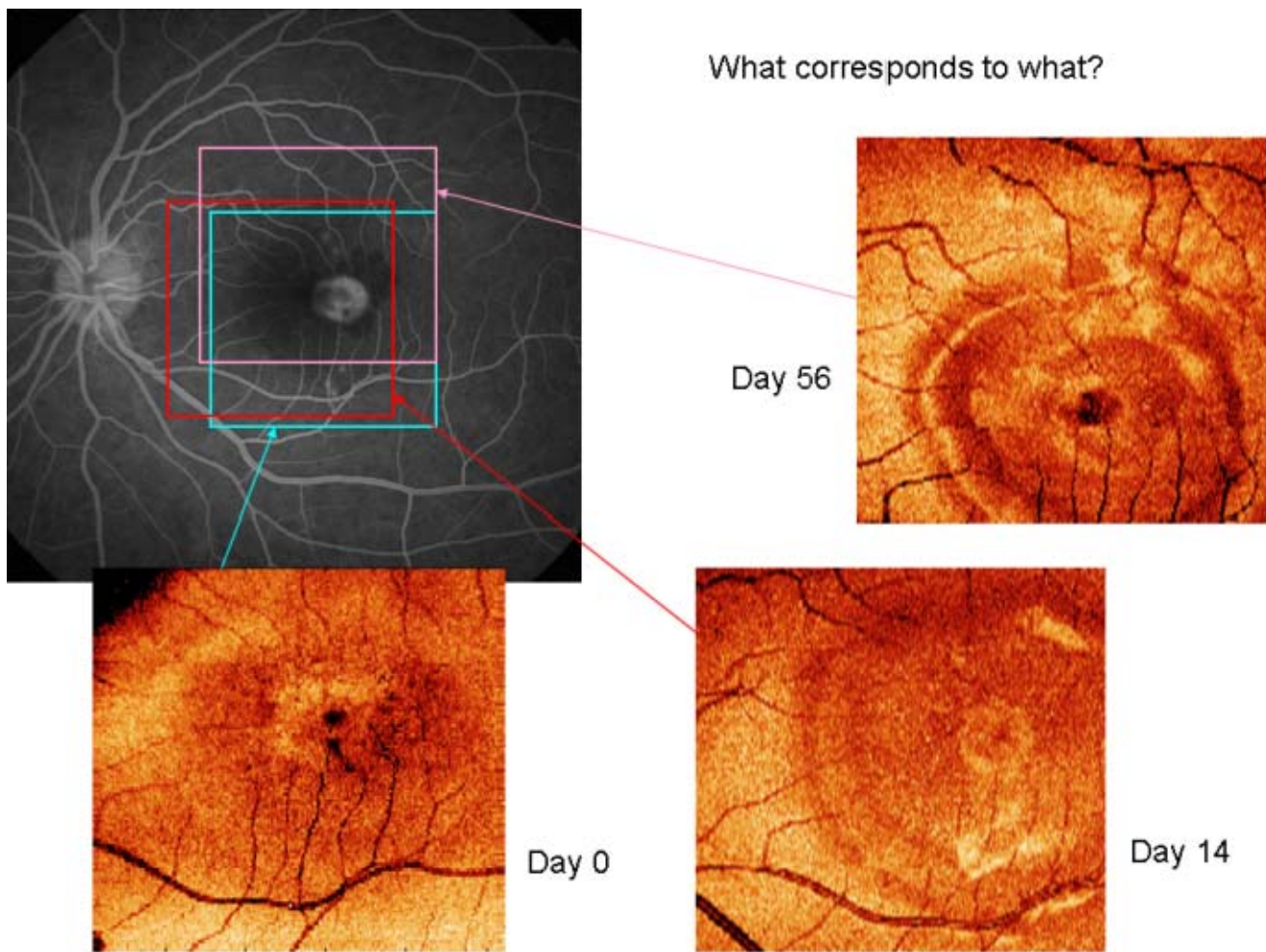
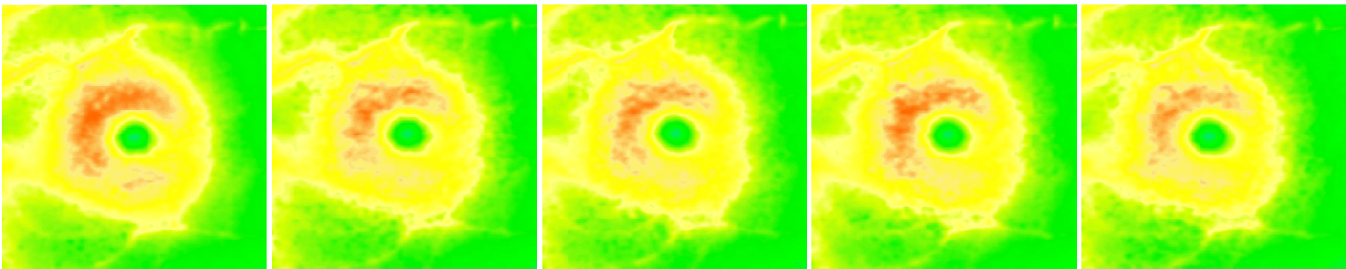
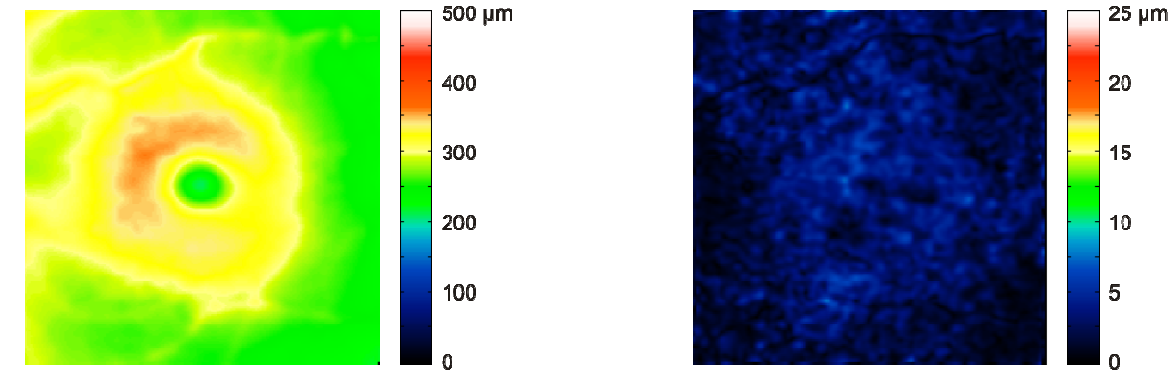


Fig. 11 Registration of OCT images can be needed to analyze reproducibility: the left eye of a patient was imaged three times over two months. Clearly the scans do not overlap exactly.

Reproducibility is excellent in normal subjects. In this case the retinal thickness changes continuously and the thickness maps can be registered in an effective manner. We see in Fig. 12 a typical example where five separate OCT datasets of a normal eye were acquired and compared after registration. The pointwise standard deviation map shows that at most pixels the standard deviation of the five thickness measurements is well below  $5\mu\text{m}$  (and always below  $8\mu\text{m}$ ). The average standard deviation is  $2.52\mu\text{m}$ .



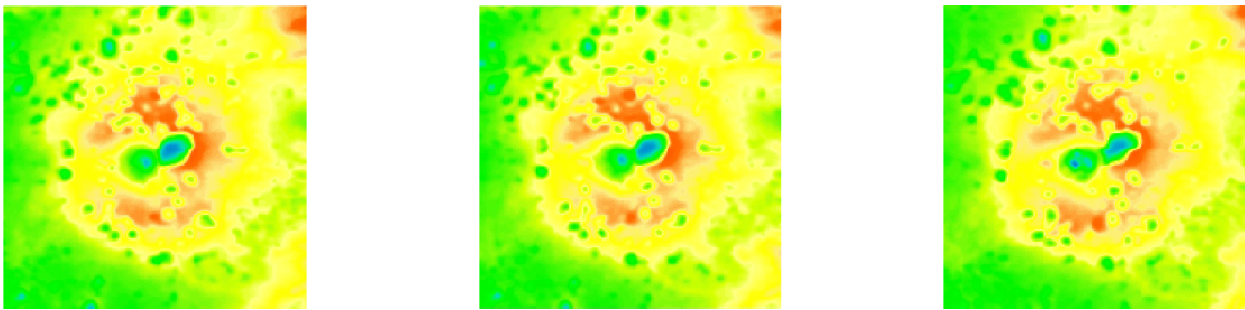
5 separate scans of the same normal eye



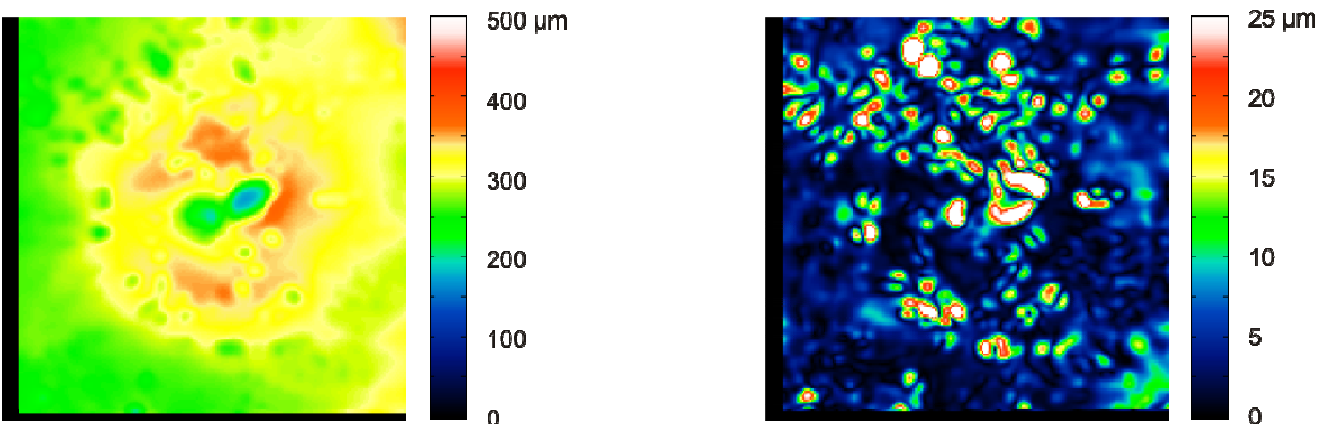
Pointwise average Retina thickness map

Pointwise standard deviation map  
Average pointwise sc=2.52  $\mu\text{m}$

Fig. 12 Reproducibility for a normal eye.



3 separate scans of an eye with dry AMD



Pointwise average Retina thickness

Pointwise standard deviation map  
Average pointwise sd=6.67  $\mu\text{m}$

Fig. 13 Reproducibility for an eye with AMD.

Fig. 9.



In the presence of pathologies the reproducibility of thickness measurements might deteriorate somewhat. The sharp, localized changes in thickness maps due to drusen, for instance, can increase the standard deviation as we see in Fig. 13. This effect may be partly due to difficulties with the registration, which in this case is particularly important and may not be as good as one would like. It should be noted that both the average thickness map and the standard deviation map show some black area along the left and lower edges. These are the areas where the three dataset fail to overlap. It might also be remarked that, while the pointwise standard deviation map show small areas with relatively large standard deviation values, the qualitative look of the three thickness maps is very close. For most clinical purposes average retinal thickness values over regions of interest might be the relevant measurement. For instance physicians are familiar with the ETDRS grid which defines nine regions bounded by three concentric circles (Fig. 10). When using the ETDRS grid to produce average retinal thickness values, the scans in Fig. 9 show a very high degree of reproducibility.

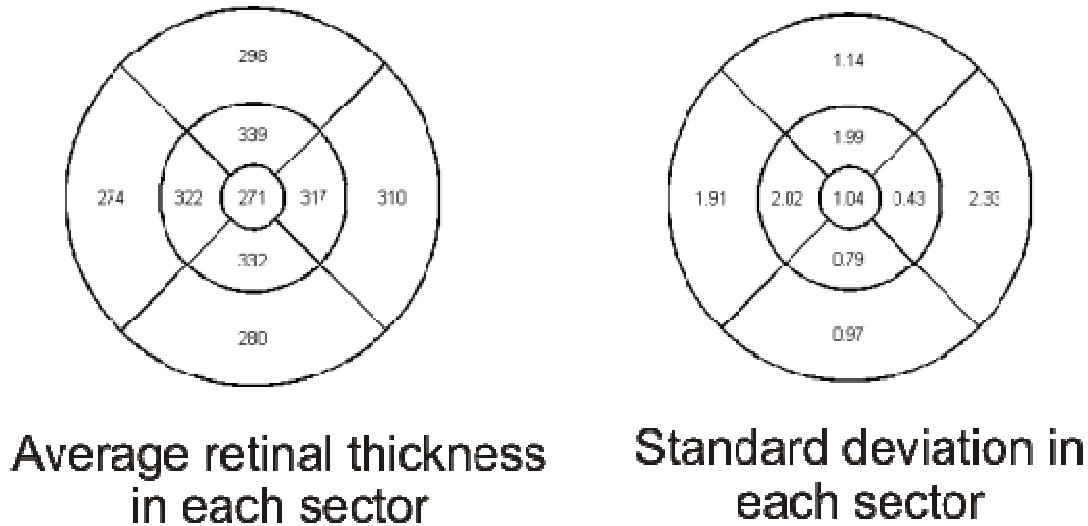


Fig. 14 Average thickness and standard deviation over the 9 ETDRS regions for the eye in Fig. 13.

The 3D datasets generated by our SD-OCT instrument can be automatically analyzed with the segmentation software we developed. This allows us to generate thickness maps consisting of 40000-70000 data points distributed over a square region of the retina. This wealth of sample points creates images that can accurately describe even small features.

The boundaries selected from the automated algorithm are generally in very good agreement point-wise with the manually drawn boundaries. In particular on diseased eyes these lines are within 20μm of each other on well over 90% of pixels about 85% of the times. It should be kept in mind that many of these eyes were seriously diseased, poor image quality was not an exclusion criteria, and different retinal specialists were often at odds on where boundaries (especially the RPE) should be drawn. The standard deviation of the probability distribution for the errors was below 10 μm, when controlling for outliers.

The variance of the segmentation of different scans of the same eye was measured at every pixel after the images were registered. This point-wise variance, as well as the mean variance, was typically well below 5 μm.

## Task 2. Develop ultra-high resolution ophthalmic OCT system.

A high-speed high resolution 3D SD-OCT was built. A schematic of the experimental system for the preliminary studies is shown in Fig. 15. In the SD-OCT system, the low-coherence light from a three-module superluminescent diode (T-840 Broadlighter, Superlum Diodes Ltd. Moscow, Russia) with center wavelength of 840 nm and FWHM bandwidth of 100 nm is coupled into an optical fiber-based Michelson interferometer. In the sample arm, the sample light is delivered to the retina by a modified optical head of an OCT 2 system (Carl Zeiss Meditec Inc., Dublin, CA). The power of the sample light was lowered to 750μW by adjusting the source power to ensure that the light intensity delivered to the eye was within the ANSI standard. In the detection arm, a spectrometer consisting of a collimating lens, a transmission grating (1200 line/mm), a multi-element imaging lens ( $f = 180$  mm), and a line scan CCD camera (Aviiva-SM2-CL-2014, 2048 pixels with 14 micron pixel size

operating in 12-bit mode) was used to detect the combined reference and sample light. The calculated spectral resolution of the spectrometer was 0.055 nm, which corresponds to a detectable imaging depth range of 3.1 mm in air. OCT scans consisting of a total number of 65536 depth scans (A-scans) takes 2.7 seconds. An image acquisition board (NI IMAQ PCI 1428) acquired the image captured by the camera and transferred it to a computer workstation (IBM IntelliStation Z Pro, dual 3.6 GHz processor, 3 GB memory) for signal processing and image display. A complete raster scan consisting of  $128 \times 512$  scanning steps took about 2.7 seconds when the A-line rate of the OCT system was set to be 24 kHz. At this operating condition, the measured sensitivity was about 95dB.

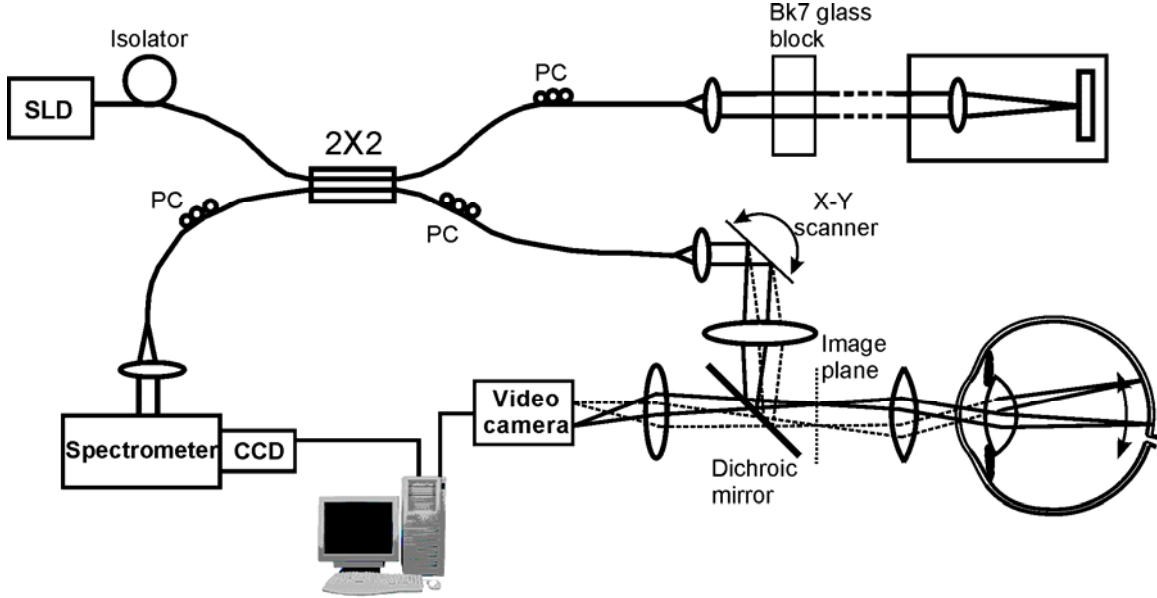


Fig. 15. Schematic of the preliminary experimental system. SLD: superluminescent diode (Broadlighter, Superlum Diodes Ltd, Moscow, Russia); PC: polarization controller. The spectrometer consists of a  $f=50$  mm collimating lens, a 1200 line/mm transmission grating and a  $f=200$  mm imaging lens. The CCD camera is a 2048 element linear array with  $14 \mu\text{m}$  element size (Aviiva-M2-CL-2014, Atmel, USA).

### Calculation of the OCT signal

In spectral-domain OCT, the combined back-reflected sample and reference light in a Michelson interferometer is detected by a spectrometer together with an array detector (usually a CCD camera). The following analyses assume that a linear array detector is used whose elements are aligned in the direction along which the spectrum is spread in the spectrometer. We also ignore the polarization effects in the interference between the reference and sample light without losing the generality of the analysis. The signal detected by the array detector is called a spectral-domain signal to distinguish it from the time-varying signal detected in a conventional time-domain OCT. The light intensity incident on each element of the line scan camera is proportional to the spectral density  $G_d(\nu)$  of the combined reference and sample light, which can be expressed as

$$G_d(\nu) = G_s(\nu) \left\{ 1 + \sum_n R_n + 2 \sum_{n \neq m} \sqrt{R_n R_m} \cos[2\pi\nu(\tau_n - \tau_m)] + 2 \sum_n \sqrt{R_n} \cos[2\pi\nu(\tau_n - \tau_r)] \right\}, \quad (1)$$

where  $\nu$  is the light frequency;  $R_n$  is the normalized intensity reflection representing the contribution to the collected sample light by the  $n$ th scatterer;  $G_s(\nu)$  is the spectral density of the light source; the reflection of the reference arm is assumed to be unity; distances are represented by propagation times  $\tau_n$ ,  $\tau_m$  of the light reflected by the  $n$ th and  $m$ th scatterers in the sample and  $\tau_r$  reflected by the reference mirror in the reference arm and summation is across all axial depths in the sample beam.

The spectral-domain signal can be transformed to the time-domain by using the Wiener-Khinchin theorem [15]:

$$\Gamma(\tau) = \langle u(t)u^*(t + \tau) \rangle = FT^{-1}[G_s(\nu)] \quad (2)$$

where  $\Gamma(\tau)$  is the autocorrelation function of the source light;  $u(t)$  is the amplitude of the electric field of the light; the angle brackets denote integration over time and  $FT^{-1}$  denotes the inverse Fourier transform. By taking an inverse Fourier transformation of Eq. (1), we obtain the time-domain intensity signal:

$$I(\tau) = \Gamma(\tau) + \Gamma(\tau) \sum_n R_n + 2 \sum_{n \neq m} \sqrt{R_n R_m} \Gamma[\tau \pm 2(\tau_n - \tau_m)] + 2 \sum_n \sqrt{R_n} \Gamma[\tau \pm 2(\tau_n - \tau_r)], \quad (3)$$

In Eqs. (1) and (3), the third terms are the mutual interference for all light scattered within the sample expressed in the frequency domain and the time domain, respectively, and the last terms contain the interference between the scattered sample light and the reference light from which an OCT A-scan is calculated [16].

The discrete Fourier transformation that yields Eq. (3) requires even sampling in  $\nu$ . In a spectrometer, however, the spectrum is evenly spread along the wavelength (here we do not consider the nonlinear terms, detailed analysis of the wavelength distribution will be discussed in 0) and the acquired raw spectrum must be interpolated to get the correct OCT signal.

### *Calculation of the OCT fundus image [17]*

The contrast in a SLO image is provided by the lateral distribution of  $\sum R_n$  across the retina. To construct a fundus intensity image from the OCT data set we need to extract the intensity term  $\sum R_n$  that is contained in both the second and fourth terms of Eqs. (1) and (3). There are multiple methods for extracting the intensity; the method selected for a particular application will depend on desired speed and accuracy.

One method is to use the non-interference terms in the frequency domain to construct the intensity image. We noticed that the cosine terms in Eq.(1) have many cycles across the spectrum and will sum to (approximately) zero, leaving only the constant terms. As a result, when we sum Eq. (1) across  $\nu$ , we have

$$F_{v1}(x, y) = \overline{G}_s \left( 1 + \sum_n R_n \right), \quad (4)$$

where  $F_{v1}(x, y)$  is the output of the processing method for an A-line at lateral scan point  $(x, y)$  on the fundus and  $\overline{G}_s$  is the total source power.

Another method to derive the fundus intensity is to use the fourth term of Eq. (1) by separating the oscillatory component of Eq. (1) from the slow variation and recognizing that, for retina and other low reflectance samples, the third term is small relative to the fourth term. One way to achieve this is first to remove the low frequency component in Eq. (1) by high pass filtering the detected spectrum, then squaring the remaining oscillatory component and summing over the spectrum. The result can be expressed as

$$F_{v2}(x, y) = \sum_\nu \left\{ 2 \sum_n \sqrt{R_n} G_s(\nu) \cos[2\pi\nu(\tau_n - \tau_r)] \right\}^2 = 4 \overline{G}_s^2 \sum_n R_n, \quad (5)$$

where  $F_{v2}(x, y)$  is the intensity calculated in the frequency domain, which can be displayed directly to produce an intensity image. According to Parseval's theorem,  $F_{v2}(x, y) = F_t(x, y)$  where  $F_t(x, y)$  is the intensity calculated in time domain.  $F_t(x, y)$  can be acquired from the calculated OCT signal in Eq. (3) by squaring and summing the values at all axial positions except those near  $\tau = 0$ . We have

$$F_t(x, y) = \sum_\tau \left\{ 2 \sum_n \sqrt{R_n} \Gamma[\tau \pm 2(\tau_n - \tau_r)] \right\}^2. \quad (6)$$

### *Wavelength distribution in the spectrometer*

In a spectral-domain OCT system the accuracy of the wavelength distribution in the spectrometer can severely affect the depth resolution of the system and the signal to noise ratio (SNR). Therefore, calibration of the wavelength distribution in the spectrometer is one important step for achieving depth resolution close to the

theoretical prediction [18]. Fig. 16 shows the simulation results on the effect of wavelength distribution error in the spectrometer on the depth resolution in spectral-domain OCT. Two boundaries with different reflectivity were simulated as the sample. Fig. 16a shows the situation when there is no error in the wavelength distribution. Fig. 16b shows the situation when the nonlinear terms in the wavelength distribution exist but were omitted. The resulted depth dependent resolution distortion can be clearly seen in the figure.

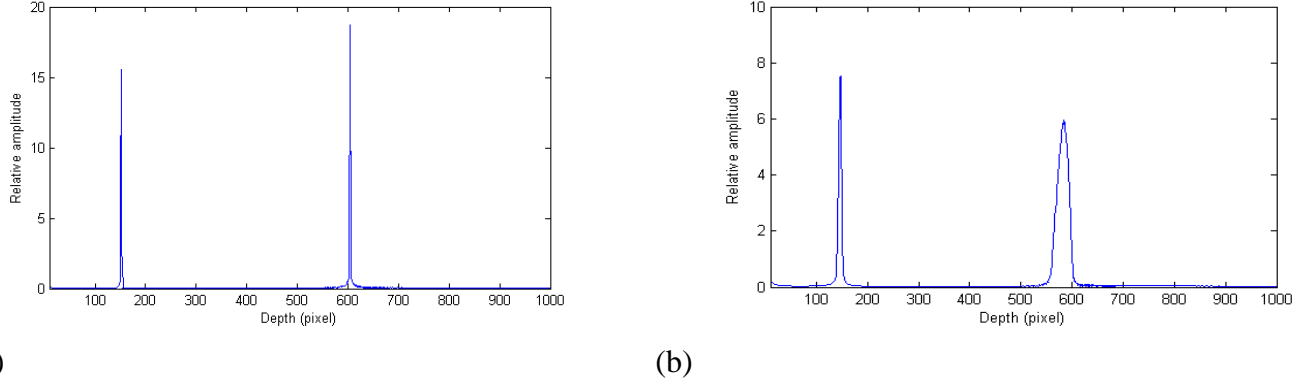


Fig. 16. Simulation of the effect of error of wavelength distribution in the spectrometer on the depth resolution in spectral-domain OCT. Two boundaries with different reflectivity were simulated as the sample. (a): there is no error in the wavelength distribution; (b): the nonlinear terms in the wavelength distribution exist but were omitted. We can see clearly the depth dependent resolution distortion in (b).

The theoretical wavelength distribution in the spectrometer can be worked out using Fig. 17a. The grating equation for the first order diffraction can be expressed as

$$\lambda = d \sin \theta_i + d \sin(\theta + \theta_i), \quad (7)$$

where  $\theta_i$  is the incident angle for the transmission grating;  $\theta_i + \theta$  is the diffraction angle for wavelength  $\lambda$ ;  $d$  is spacing of the grooves of the grating. Assuming that the center wavelength of the light source falls on the center pixel of the CCD camera the wavelength distribution on the CCD camera can be expressed as

$$\begin{aligned} \lambda &= \frac{\lambda_0}{2} + \frac{dx/f \cos \theta_i}{\sqrt{1 + (\frac{x}{f})^2}} + \frac{d \sin \theta_i}{\sqrt{1 + (\frac{x}{f})^2}} \approx \lambda_0 + d \frac{x}{f} \cos \theta_i - \frac{d}{2} \left(\frac{x}{f}\right)^2 \sin \theta_i - \frac{d}{2} \left(\frac{x}{f}\right)^3 \cos \theta_i, \\ &= \lambda_0 + a_1(x_d - V_m/2) - a_2(x_d - V_m/2)^2 - a_3(x_d - V_m/2)^3 \end{aligned} \quad (8)$$

where  $\lambda_0$  is the center wavelength of the light source;  $x$  is the distance on the CCD imaging plane from the center;  $f$  is focal length of the imaging lens;  $a_1$ ,  $a_2$ , and  $a_3$  are coefficients for the first order, second order, and third order terms;  $x_d$  and  $V_m$  are the pixel number and the maximal pixel number of the CCD camera,  $0 \leq x_d \leq V_m$ .



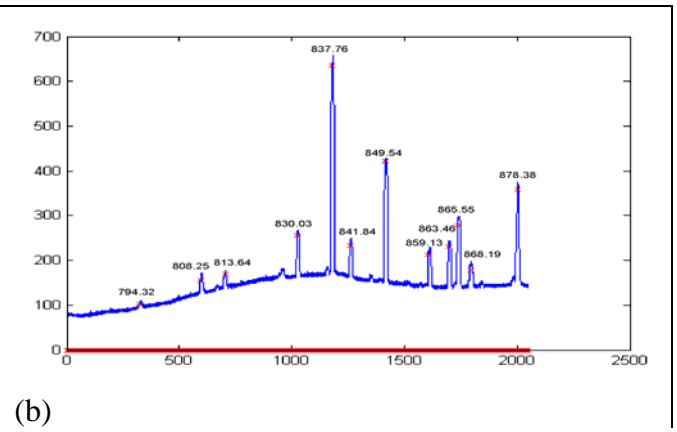
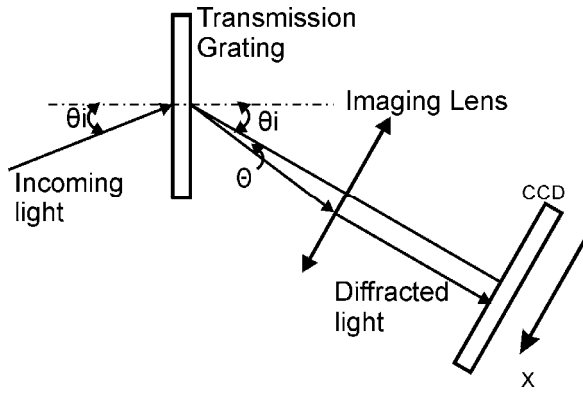


Fig. 17. (a) Illustration of the light diffraction in the spectrometer.  $\theta_i$  is the incident angle of the incoming light. The configuration of the system meets the Littrow condition.  $\theta$  is the diffraction angle in reference to the center wavelength. (b) An example for the spectrometer calibration: the position for each atomic line predicted by the theoretical model (\*) was compared with the measured spectrum of a Neon spectral lamp.

Fig. 17b shows one example of the spectrometer calibration using a Neon spectral calibration lamp (6032, Newport Corporation), where the position of each atomic line predicted by the theoretical model (\*) in the figure) was compared with the measured spectrum of the lamp. In this example the measured position of each atomic line of the spectral lamp matched the theoretical model preferably. When errors occur, the coefficients  $a_1$ ,  $a_2$ , and  $a_3$  need to be tuned.

To further eliminate any effect from the possible residual error in the wavelength distribution after calibration with the spectral lamp a method reported in by C. Dorrer [18] will be employed. Namely we can use a mirror in the sample arm and measure the spectral interferogram with different delays. By curve fitting on the phase differences for different delay differences the non-linear term in the wavelength calibration error can be extracted and then eliminated during signal processing for OCT imaging.

### Dispersion compensation

Dispersion is caused by the dependence of the refractive index of the optical medium on the optical frequency. In a dispersive optical medium light of different wavelengths travels at different speed. Dispersion mismatch between the sample and reference arms in an interferometer causes distortions to the point spread function, then the depth resolution, of the system. Dispersion between the two arms in an interferometer needs to be carefully matched in the entire bandwidth of the broadband light source in order to achieve optimal depth resolution in an ultra-high resolution OCT [19]. Dispersion in the sample arm in retinal OCT imaging is predominantly attributed to the media in front of the retina including the ocular tissue and optical materials in the sample arm. As a result, dispersion variation in the entire imaging range is negligible [20].

In spectral-domain OCT dispersion mismatch between the sample and reference arms can be compensated during signal processing. The phase of the interferogram for each axial scan can be expressed as

$$\Phi(\omega) = \Phi_0 + c_1(\omega - \omega_0) + c_2(\omega - \omega_0)^2 + c_3(\omega - \omega_0)^3, \quad (9)$$

where  $\omega_0$  is the center angular frequency of the light source. The first order term (the second term) is the OCT signal. The second and third order terms (the third and fourth terms) are caused by the second and third order dispersion mismatch between the two arms. To compensate for the dispersion mismatch we can construct a complex compensation phase function:

$$G_c(\omega) = \exp[-ic_2'(\omega - \omega_0)^2 - ic_3'(\omega - \omega_0)^3]. \quad (10)$$

After removing the DC terms in the detected interferogram expressed in Eq. (1) we multiply the signal with

$G_c(\omega)$  and we have

$$\begin{aligned}
G_c(\omega)G_d(\omega) &= \exp[-ic_2'(\omega - \omega_0)^2 - ic_3'(\omega - \omega_0)^3] 2 \sum_n \sqrt{R_n} \cos[\omega(\tau_n - \tau_r) + c_2(\omega - \omega_0)^2 + c_3(\omega - \omega_0)^3] \\
&= \sum_n \sqrt{R_n} \exp[i\omega(\tau_n - \tau_r) + i(c_2 - c_2')(\omega - \omega_0)^2 + (c_3 - c_3')(\omega - \omega_0)^3] \\
&\quad + \sum_n \sqrt{R_n} \exp[i\omega(\tau_n - \tau_r) + i(c_2 + c_2')(\omega - \omega_0)^2 + (c_3 + c_3')(\omega - \omega_0)^3]
\end{aligned} \tag{11}$$

where we omitted the initial phase. When  $c_2' = c_2$  and  $c_3' = c_3$ , by taking the inverse Fourier transformation we have

$$\begin{aligned}
FT^{-1}[G_c(\omega)G_d(\omega)] &= FT^{-1} \left\{ \sum_n \sqrt{R_n} \exp[i\omega(\tau_n - \tau_r)] \right\} \\
&\quad + FT^{-1} \left\{ \sum_n \sqrt{R_n} \exp[i\omega(\tau_n - \tau_r) + 2ic_2(\omega - \omega_0)^2 + 2ic_3(\omega - \omega_0)^3] \right\}.
\end{aligned} \tag{12}$$

The first term in the expression is the dispersion free OCT signal while the second term is the mirror image in which the dispersion is doubled. With this method the real image is compensated for the dispersion mismatch while the mirror image is blurred, which has the additional advantage for discriminating the real image from its mirror for the operator.

An iterative algorithm similar to the one used by M. Wojtkowski et al [20] for finding the correct coefficients for  $c_2 = c_2'$  and  $c_3 = c_3'$  will be used. The task of the algorithm is to find the two coefficients that make the energy in each axial scan the most concentrated, i.e. the image is the sharpest. The flowchart for the procedure of dispersion compensation is shown in Fig. 18. In the procedure the last zero padding is to ensure that after the inverse Fourier transformation the pixel spacing is smaller than half of the designed depth resolution. The algorithm eliminated the process for calculating the phase of the signal thus avoided the possible unwrapping error.

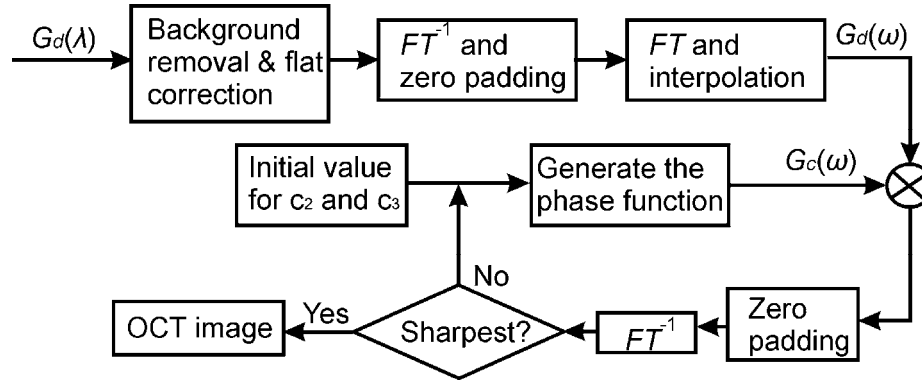


Fig. 18. Flow chart for the iterative dispersion compensation procedure. The iteration continues until the OCT signal is the sharpest measured with the sharpness metric. Usually the processes for finding the second and third order compensation coefficients are separated. The last zero padding is to ensure that after the inverse Fourier transformation the pixel spacing is smaller than half of the designed depth resolution.

As shown in Fig. 19, the calibrated depth resolution is 3.8  $\mu\text{m}$  in air and  $\sim 3\mu\text{m}$  the tissue, which was corrected with the refractive index of biological tissues ( $\sim 1.4$ ).

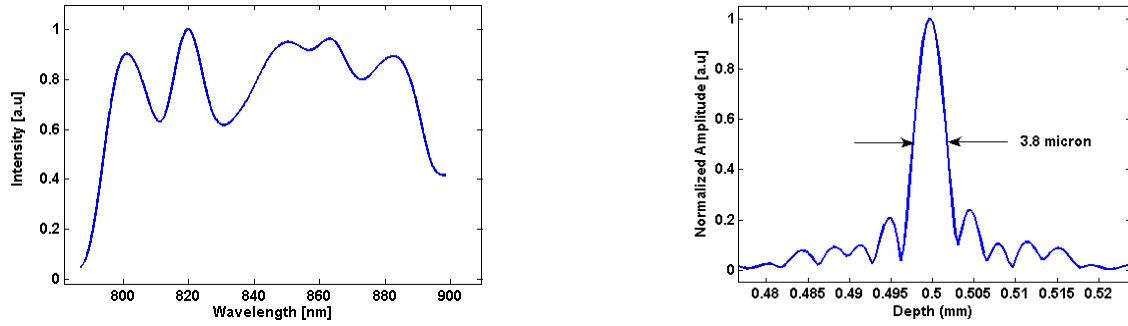


Fig. 19. measured spectrum of the light source and the point-spread function of the ultra-high resolution OCT.

### *Test the OCT system on normal human eye*

The OCT system was tested on imaging normal human eye (the PI's eye). Fig. 20 shows the OCT image of a normal human retina. From the image we can see that all the sub-retinal layers can be seen clearly, which demonstrated the resolving capability of the ultra-high resolution OCT system.

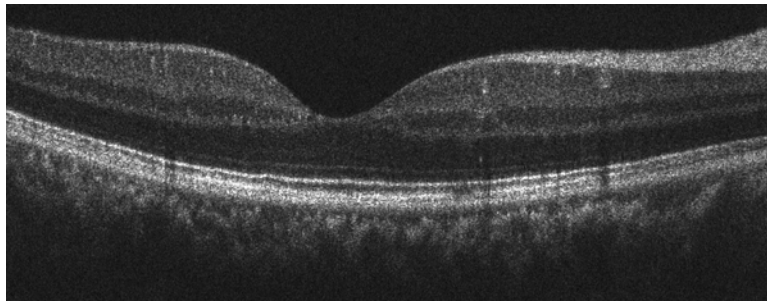


Fig. 20. OCT image of the normal human retina.

By adding switchable optics in the sample arm, the OCT system was capable of imaging both the anterior segments and the retina of the eye. Fig. 21 shows the acquired images of the cornea and conjunctiva of a normal eye with contact lenses. By adding artificial tears and after several blinks the OCT system can not only reveal the pre-lens and post-lens tear films but also all the details of the anatomy of the cornea: the corneal epithelium, basal cell layer, Bowman's membrane, stroma, and endothelium.

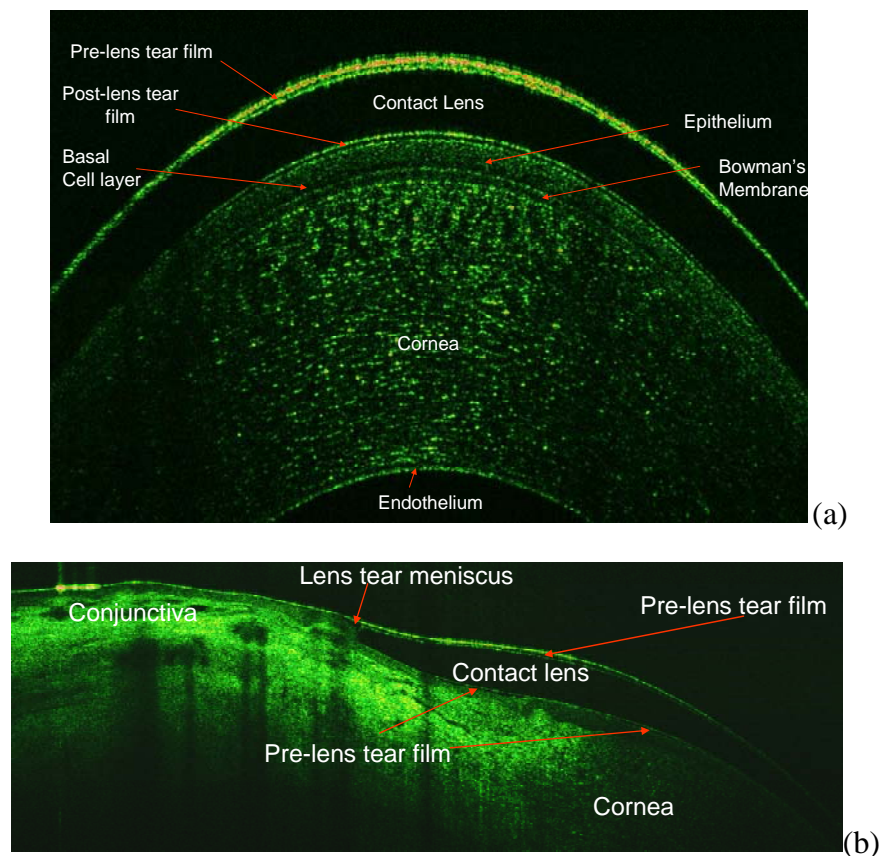


Fig. 21 OCT images of the anterior segment of the eye. (a) a magnified view of the cornea with soft contact lens; (b) image of the conjunctiva with soft contact lens.

## KEY RESEARCH ACCOMPLISHMENTS

- Developed methods for accurate vertical alignment and matching, including the overlay of a color or red-free, fundus photograph on an OCT image for registration.
- Developed the mathematical algorithms to analyze and quantify OCT datasets automatically including 3D segmentation algorithm for quantitative mapping of the retinal thickness using 3D OCT data for normal and diseased human eyes.
- Tested the accuracy of the segmentation algorithm by comparing the segmentation results done by the algorithm and by experts, respectively.
- Further improved the resolution of the spectral OCT. The developed OCT system has a depth resolution of  $\sim 3 \mu\text{m}$  in tissue and is capable of resolving all the sub-retinal features of the retina.

## REPORTABLE OUTCOMES

### *Journal article*

1). H. Wehbe, M. Ruggeri, S. Jiao, G. Gregori, C. A. Puliafito, and W. Zhao, "Automatic retinal blood flow calculation using spectral domain optical coherence tomography," Opt. Express 15, 15193-15206 (2007).  
<http://www.opticsinfobase.org/abstract.cfm?URI=oe-15-23-15193>.

- 1). S. Jiao, J. Wang, and C. A. Puliafito, "Contrast Enhancement for Imaging the Tears and Contact Lens with Optical Coherence Tomography", ARVO 2008.
- 2). H.M. Wehbe, M. Ruggeri, S. Jiao, C. Puliafito, "Quantitative Retinal Blood Flow Measurement and Calibration Using Spectral Domain Optical Coherence Tomography", ARVO 2008.

## CONCLUSION

High resolution OCT images can reveal the detailed anatomical structures of both the anterior and posterior segments of the eye. Ultra-high resolution SD-OCT provides a powerful tool for visualizing the 3D microscopic structures of the eye *in vivo*. Incorporating with segmentation algorithms quantitative information like the 3D geometry of the retina, retinal thickness map, and tear volume can be extracted from the measured OCT images, which make possible more objective quantitative evaluation of eye diseases. It will also simplify and accelerate diagnosis and monitoring of retinal disease by enabling prompt triage and therapy implementation by optometrists and non-ophthalmologist physicians. The development of registration algorithms makes possible more accurate evaluation of images taken at progressive intervals, which will better enable ophthalmologists to follow the course of the disease and its treatment. Furthermore, improved resolution of SD-OCT will enable telemedicine consultation on retinal disease for non-ophthalmologist health professionals, potentially preventing vision loss and blindness. Next step of the study should be focused on optimization of the system hardware and registration software to make it more stable and robust.

## REFERENCES

1. B. Zitova and J. Flusser, "Image registration methods: a survey", *Image and Vision Computing* **21**, 977-1000 (2003).
2. J. B. A. Maintz and M. A. Viergever, "A survey of medical image registration", *Med. Image Anal.* **2**, 1-36 (1998).
3. M. S. Mabrouk, N. H. Solouma, and Y. M. Kadah, "Survey of retinal image segmentation and registration", *GVIP Journal* **6**, 1-11 (2006).
4. G. K. Matsopoulos, N. A. Mouravliansky, K. K. Delibasis, and K. S. Nikita, "Automatic retinal image registration scheme using global optimization techniques", *IEEE Trans. Inf. Technol. Biomed.* **3**, 47-60 (1999).
5. T. Chanwimaluang, G. Fan, and S. R. Fransen, "Hybrid retinal image registration", *IEEE Trans. Inf. Technol. Biomed.* **10**, 129-142 (2006).
6. A. Can, C. V. Stewart, B. Roysam, and H. L. Tanenbaum, "A feature-based, robust, hierarchical algorithm for registering pairs of images of the curved human retina", *IEEE Trans. PAMI* **24**, 347-364 (2002).
7. C. V. Stewart, C. L. Tsai, and B. Roysam, "The dual-bootstrap iterative closest point algorithm with application to retinal image registration", *IEEE Trans. Med. Imag.* **22**, 1379-1394 (2003).
8. C. L. Tsai, C. V. Stewart, H. L. Tanenbaum, and B. Roysam, "Model-based method for improving the accuracy and repeatability of estimating vascular bifurcations and crossovers from retinal fundus images", *IEEE Trans. Inf. Technol. Biomed.* **8**, 122-130 (1996).
9. J. B. A. Maintz, P. A. van den Elsen, and M. A. Viergever, "Evaluation of ridge seeking operators for multimodality medical image matching", *IEEE Trans. PAMI* **18**, 353-365 (1996).

10. J. Staal, M. D. Abramoff, M. Niemeijer, M. A. Viergever, and B. van Ginneken, "Ridge-based vessel segmentation in color images of the retina", *IEEE Trans. Med. Imaging* **23**, 501-509 (2004).
11. D. P. Huttenlocher, G. A. Klanderman, and W. J. Rucklidge, "Comparing images using the Hausdorff distance", *IEEE Trans. PAMI* **15**, 850-863 (1993).
12. P. J. Besl and H. D. McKay, "A method for registration of 3-D shapes", *IEEE Trans. PAMI* **14**, 239-256 (1992).
13. S. Rusinkiewicz and M. Levoy, "Efficient variants of the ICP algorithm", *IEEE Intl. Conf. on 3-D Digital Imaging and Modeling*, Quebec, 145-152 (2001).
14. P. Thevenaz, U. E. Ruttimann, and M. Unser, "A pyramid approach to subpixel registration based on intensity", *IEEE Trans. Image Processing* **7**, 27-41 (1998).
15. J. W. Goodman, *Statistical Optics*, Wiley, New York (1985).
16. A. F. Fercher, C. K. Hitzenberger, G. Kamp, and S. Y. El-Zaiat, "Measurement of intraocular distances by backscattering spectral interferometry," *Optics Communications* **117**, 43-48 (1995).
17. S. Jiao, R. Knighton, X. Huang, G. Gregori, and C. A. Puliafito, "Simultaneous acquisition of sectional and fundus ophthalmic images with spectral-domain optical coherence tomography", *Opt. Express* **13**, 444-452 (2005), <http://www.opticsexpress.org/abstract.cfm?URI=OPEX-13-2-444>.
18. C. Dorrer, "Influence of the calibration of the detector on spectral interferometry," *J. Opt. Soc. Am. B* **16**, 1160-1168 (1999).
19. C. K. Hitzenberger, A. Baumgartner, W. Drexler, and A. F. Fercher, "Dispersion effects in partial coherence interferometry: implications for intraocular ranging," *J. Biomed. Opt.* **4**, 144-151 (1999).
20. M. Wojtkowski, V. J. Srinivasan, T. H. Ko, J. G. Fujimoto, A. Kowalczyk, and J. S. Duker, "Ultrahigh-resolution, high-speed, Fourier domain optical coherence tomography and methods for dispersion compensation," *Opt. Express* **12**, 2404-2422 (2004), <http://www.opticsexpress.org/abstract.cfm?URI=OPEX-12-11-2404>.



# Automatic retinal blood flow calculation using spectral domain optical coherence tomography

Hassan Wehbe<sup>1,2</sup>, Marco Ruggeri<sup>1</sup>, Shuliang Jiao<sup>1</sup>, Giovanni Gregori<sup>1</sup>  
Carmen A. Puliafito<sup>1</sup> and Weizhao Zhao<sup>2</sup>

<sup>1</sup>Bascom Palmer Eye Institute, University of Miami Miller School of Medicine, 1638 NW 10th Ave, Miami, FL 33136

<sup>2</sup>Department of Biomedical Engineering, University of Miami, Coral Gables, FL 33124-0621

[sjiao@med.miami.edu](mailto:sjiao@med.miami.edu); <http://www.bpei.med.miami.edu>

**Abstract:** Optical Doppler tomography (ODT) is a branch of optical coherence tomography (OCT) that can measure the speed of a blood flow by measuring the Doppler shift impinged on the probing sample light by the moving blood cells. However, the measured speed of blood flow is a function of the Doppler angle, which needs to be determined in order to calculate the absolute velocity of the blood flow inside a vessel. We developed a technique that can extract the Doppler angle from the 3D data measured with spectral-domain OCT, which needs to extract the lateral and depth coordinates of a vessel in each measured ODT and OCT image. The lateral coordinates and the diameter of a blood vessel were first extracted in each OCT structural image by using the technique of blood vessel shadowgram, a technique first developed by us for enhancing the retinal blood vessel contrast in the *en face* view of the 3D OCT. The depth coordinate of a vessel was then determined by using a circular averaging filter moving in the depth direction along the axis passing through the vessel center in the ODT image. The Doppler angle was then calculated from the extracted coordinates of the blood vessel. The technique was applied in blood flow measurements in retinal blood vessels, which has potential impact on the study and diagnosis of blinding diseases like glaucoma.

©2007 Optical Society of America

OCIS codes: (110.4500) Optical coherence tomography; (120.3890) medical optics instrumentation; (170.4580) optical diagnostics for medicine.

## References and links

1. J. Flammer, S. Orgül, V. P. Costa, N. Orzalesi, G. K. Kriegelstein, L. M. Serra, J. P. Renard, and E. Stefánsson, "The impact of ocular blood flow in glaucoma," *Prog. Retinal Res.* **21**, 359–393 (2002).
2. R. Allingham, K. Damji, S. Freedman, S. Moroi, G. Shafranov, M. Shields, *Shields' textbook of glaucoma*, Fifth Edition, (Lippincott Williams & Wilkins, 2005).
3. E. Dienstbier, J. Balik and H. Kafka, "A contribution to the theory of the vascular theory of glaucoma," *Br. J. Ophthalmol.* **34**, 47–58 (1950).
4. H. Ren, K. M. Brecke, Z. Ding, Y. Zhao, J. S. Nelson, and Z. Chen, "Imaging and quantifying transverse flow velocity with the Doppler bandwidth in a phase-resolved functional optical coherence tomography," *Opt. Lett.* **27**, 409–411 (2002).
5. T. G. van Leeuwen, M. D. Kulkarni, S. Yazdanfar, A. M. Rollins, and J. A. Izatt, "High-flow-velocity and shear-rate imaging by use of color Doppler optical coherence tomography," *Opt. Lett.* **24**, 1584–1586 (1999).
6. H. Wehbe, M. Ruggeri, S. Jiao, G. Gregori, C. Puliafito "Automatic retinal blood vessel parameter calculation in spectral domain optical coherence tomography," *Proc. SPIE*, **6429** 64290D (2007).
7. V. X. D. Yang, M. L. Gordon, A. Mok, Y. Zhao, Z. Chen, R. Cobbold, B. Wilson, and I. Vitkin, "Improved phase resolved optical Doppler tomography using the kasai velocity estimator and histogram segmentation," *Opt. Commun.* **208**, 209–214 (2002).
8. J. Schuman, T. Pedut-Kloizman, E. Hertzmark, M. Hee, J. Wilkins, J. Coker, C. Puliafito, J. Fujimoto, and E. Swanson "Reproducibility of nerve fiber layer thickness measurements using optical coherence Tomography," *Ophthalmol.* **103**, 1889–1898 (1996).

9. E. Blumenthal, J. Williams, R. Weinreb, C. Girkin, C. Berry, "Reproducibility of Nerve Fiber Layer Thickness Measurements by use of Optical Coherence Tomography," *Ophthalmol.* **107**, 2278-2282 (2000).
10. V. Guedes, J. Schuman, E. Hertzmark, G. Wollstein, A. Correnti, R. Mancini, D. Lederer, S. Voskanyan, L. Velazquez, H. Pakter, T. Pedut-Kloizman, J. G. Fujimoto, C. Mattox, "Optical Coherence Tomography Measurement of Macular and Nerve Fiber Layer Thickness in Normal and Glaucomatous Human Eyes," *Ophthalmol.* **110**, 177-189 (2003).
- S. Jiao, R. Knighton, X. Huang, G. Gregori, and C. A. Puliafito, "Simultaneous acquisition of sectional and fundus ophthalmic images with spectral-domain optical coherence tomography," *Opt. Express* **13**, 444-452 (2005).
11. A. Weber, M. Cheney, Q. Smithwick, and A. Elsner, "Polarimetric imaging and blood vessel quantification," *Opt. Express* **12**, 5178-5190 (2004).
12. A. Yoshida, G. Feke, F. Mori, T. Nagaoka, N. Fujio, H. Ogasawara, S. Konno, and J. Mcmeel, "Reproducibility and clinical application of a newly developed stabilized retinal laser Doppler instrument," *Am. J. Ophthalmol.* **136**, 404-404 (2003).

## 1. Introduction:

Glaucoma is one of the leading causes of blindness in the world and is usually associated with increased intraocular pressure (IOP). There are two theories for the pathogenesis of glaucomatous optic neuropathy (GON): the mechanical and the vascular theory, both of which have been the debate subject of multiple research groups throughout the past 150 years. [1,2-3] The vascular theory considers GON to be the result of ischemia caused by the elevated IOP or other risk factors obstructing the blood flow. A tool providing accurate quantitative structural and blood flow information will benefit the study of the etiology of glaucoma as well as the developments of new therapies by monitoring the treatment effects non-invasively. Optical Doppler tomography (ODT) is a branch of optical coherence tomography (OCT) that can measure the spatially resolved speed of a blood flow by measuring the Doppler shift caused by the moving blood cells to the probing sample light. [4,5] The measured Doppler shift ( $f_d$ ) is related to the velocity by:

$$f_d = \frac{2nv_a}{\lambda_0} \cos \theta, \quad (1)$$

where  $v_a$  is the absolute velocity of the moving blood cells,  $\lambda_0$  is the center wavelength of the light source,  $n$  is the refractive index of the sample and  $\theta$  is the Doppler angle. From the above equation it is clear that the calculated velocity from the measured Doppler shift is the projection of the absolute velocity on the direction of the incident probing light. Accordingly, in order to calculate the absolute velocity from the measured Doppler shift we need to know the Doppler angle  $\theta$ . However  $\theta$  is not only an unknown parameter in retinal ODT imaging but also changes at different imaging time.

Spectral-domain optical coherence tomography (SD-OCT) is a recently developed high speed OCT technology that provides high resolution three dimensional imaging of biological tissues. SD-OCT provides the means of calculating the Doppler angle from the acquired 3D data, which provides structural (3D orientations and the blood vessel diameters) and Doppler information of the retinal blood vessels. [6] In this paper we report on our study on the automatic extraction of the parameters of the retinal blood vessels from the images acquired with a high resolution high speed SD-OCT. The retinal blood flow can be calculated upon acquisition of these parameters together with the Doppler information.

## 2. Materials and methods

### 2.1 Ultra high resolution OCT system

A high-speed high resolution 3D SD-OCT was built for the investigation. In the SD-OCT system, the low-coherence light from a three-module superluminescent diode (T-840



Broadlighter, Superlum Diodes Ltd. Moscow, Russia) with center wavelength of 840 nm and FWHM bandwidth of 100 nm is coupled into an optical fiber-based Michelson interferometer. In the sample arm, the sample light is delivered to the retina by a modified optical head of an OCT 2 system (Carl Zeiss Meditec Inc., Dublin, CA). In the detection arm, a spectrometer consisting of a collimating lens, a transmission grating (1200 line/mm), a multi-element imaging lens ( $f = 180$  mm), and a line scan CCD camera (Aviiva-SM2-CL-2014, 2048 pixels with 14 micron pixel size operating in 12-bit mode) was used to detect the combined reference and sample light. The calculated spectral resolution of the spectrometer was 0.055 nm, which corresponds to a detectable imaging depth range of 3.1 mm in air. The calibrated depth resolution in the tissue is  $\sim 3\mu\text{m}$ , which was corrected with the refractive index of biological tissues. The power of the sample light was lowered to  $750\mu\text{W}$  by adjusting the source power to ensure that the light intensity delivered to the eye was within the ANSI standard. OCT scans consisting of a total number of 65536 depth scans (A-scans) takes 2.7 seconds.

## 2.2 Doppler imaging

The measured raw spectral interference signals were processed by using the standard algorithm for spectral domain OCT to get the complex signal  $[\Gamma(t)]$  in the time domain. To calculate the Doppler shift we first calculated the product of the complex signals for the adjacent A-lines:

$$\Gamma_{i+1}(t) \bullet \Gamma_i^*(t) = A(t)e^{i[\varphi_{i+1}(t) - \varphi_i(t)]} \quad (2)$$

where  $\Gamma^*(t)$  is the complex conjugate of  $\Gamma(t)$ ;  $A$  is the amplitude of the product;  $\varphi_i$  is the phase of  $\Gamma_i(t)$ ;  $i$  is the A-line number. The phase difference among the adjacent A-lines  $\Delta\varphi_i = \varphi_{i+1} - \varphi_i$  can then be calculated. Calculating the phase difference with Eq. (2) has the advantage of avoiding the problem of phase unwrapping.

The projected flow speed on the direction of the incident sample light can be calculated from  $\Delta\varphi_i$ :

$$v_p = \frac{\Delta\varphi_i \lambda_0 f_{A\text{-line}}}{4\pi n}, \quad -\pi \leq \Delta\varphi_i \leq \pi, \quad -\frac{\lambda_0 f_{A\text{-line}}}{4n} \leq v_p \leq \frac{\lambda_0 f_{A\text{-line}}}{4n}, \quad (3)$$

where  $v_p$  is the projection of the absolute velocity  $v_a$  along the depth direction,  $\lambda_0$  is the center wavelength of the light source (840 nm),  $f_{A\text{-line}}$  is the axial scan frequency (24000 A-lines/sec),  $n$  is the index of refraction of the sample ( $\sim 1.4$ ). Accordingly, the maximal speed that can be detected by our system without phase wrapping is  $\pm 3.6$  mm/sec.

The Doppler image contains bulk motion artifacts that is additive to the Doppler shift induced by the blood flow. Bulk motion effect can be quantified for each A-line by using the histogram technique [7]. Briefly speaking, the histogram  $H(\Delta\varphi_i)$  of the phase difference  $\Delta\varphi_i$  was calculated along each individual line of the Doppler image.  $H(\Delta\varphi_i)$  contained  $N$  bins varying in the interval  $[-\pi, \pi]$  with a step size of  $\Delta\varphi_h = \frac{\Delta\varphi_{\max} - \Delta\varphi_{\min}}{N}$ , where  $\Delta\varphi_{\max}$  and  $\Delta\varphi_{\min}$  are the maximum and minimum of  $\Delta\varphi_i$ , respectively. The phase shift  $\Delta\varphi_{\text{bulk}}$  caused by bulk motion was obtained by locating the peak of the histogram

$$\Delta\varphi_{\text{bulk}} = \max[H(\Delta\varphi_i)], \quad -\pi < H(\Delta\varphi_i) < \pi \quad (4)$$

$\Delta\phi_{bulk}$  is subtracted from its corresponding  $\Delta\phi_i$  to compensate for the bulk motion artifact for each line of the ODT image.

### 2.3 Scan patterns and eye movement compensation

The first scan pattern we used for the study is a set of evenly spaced concentric circles around the optic disk of the eye. This scan pattern was chosen to cover all major retinal arteries and veins. This scan pattern was used to test the algorithms for blood vessel detection. As illustrated in Fig. 1(a), the circular scan pattern consisted of 56 normal density (1024) and one high density (8192) depth scans (A-lines). The radius of the circles spanned evenly from 0.73 to 2.73mm on the fundus. The high density scan had a scan radius of 1.73mm, which is the same as that used in the commercial time-domain OCT machine for glaucoma imaging.[8]. A donut shaped *en face* OCT fundus image [11] can be generated and registered on the corresponding fundus photograph for the same eye. By comparing the OCT fundus image and the fundus photograph arteries and veins can be recognized. An ODT image can be generated from the high density scan. The ODT image helps not only verify the accuracy of the calculation of the lateral coordinates of each recognizable blood vessel but also locate the depth coordinate of each blood vessel on the high density OCT image.

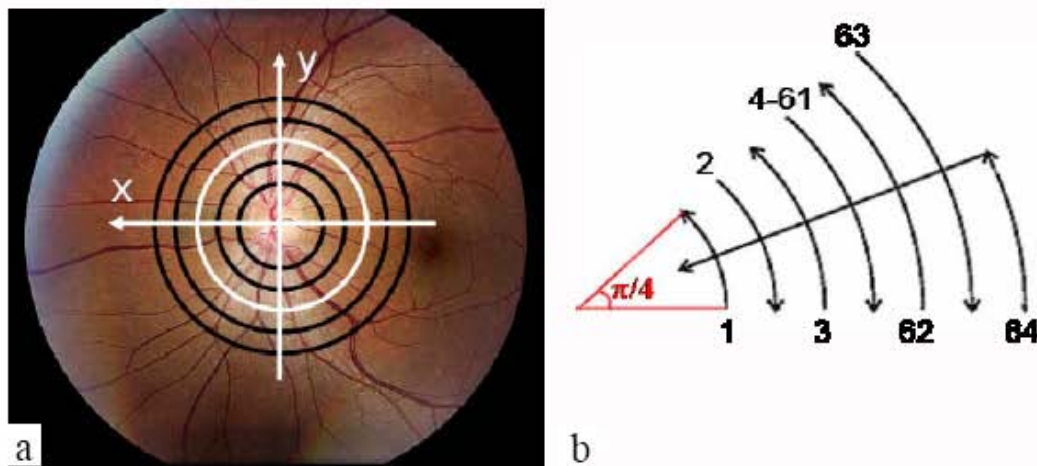


Fig. 1. (a). Circular scan pattern centered on the optic disk. The black circles represent the normal density scans (1024 A-lines); the white circle represent the high density scan (8192 A-lines). (b) Arc scan pattern. Scans 1,2,3,62,63 are used to calculate the Doppler angle. Scan 64 is used for alignment. Scans 4-61 were scanning the same area.

Another scan pattern we used is arc shaped [Fig. 1(b)] for imaging individual blood vessels. The scan pattern consisted of 63 concentric arcs, each of which has 1024 A-lines, subtending an angle of  $\pi/4$  with a radius spanning from 1.48 to 1.98mm, and one depth alignment scan (reference scan, scan No.64) for eye movement compensation. 58 scans (scan No.4 to No.61) were repeated at a radius of 1.73 mm. This arrangement of the scans is used to calculate the Doppler angle and the flow dynamics. A Doppler image was calculated for each of the arc scans, therefore allowing accurate 3D coordinate calculations.

Also illustrated in Fig. 1(a) is the coordinate system we used for the entire study, where the X-axis represents the horizontal position, the Y-axis represents the vertical position, and the Z-axis represents the depth position. We also defined  $r$  ( $1.48mm \leq r \leq 1.98mm$ ) as the scan radius and  $\alpha$  ( $0 \leq \alpha \leq 2\pi$ ) as the scan angle, both can be pre-determined by the scan data. For each pixel on the circular OCT image the lateral coordinates ( $x, y$ ) can be calculated as  $x = r \cos \alpha$  and  $y = r \sin \alpha$ .



Involuntary eye movements during image acquisition can cause distortions to the retinal OCT images as well as the locations of retinal vessels due to limited imaging speed, which in turn add an error to the Doppler angle calculation. The ultimate solution to this problem is to increase the imaging speed. With current commercially available cameras for the spectrometer, the space for improving imaging speed is very limited. As a result, compensation for the distortions caused by eye movements with post-processing is necessary. To compensate for the eye movements a linear fast reference scan crossing all the arc scans was added at the end of the arc scan. During the fast linear scan eye movement can usually be neglected, the linear scan provides a reference for all the arc scan images in the depth direction. The depth position for each arc scan can be adjusted according to this reference scan and thus provides compensation in the depth direction. Compensation according to the reference scan image can be done in different ways. In one method we can detect the front surface of all the images and each B-scan will be shifted in the Z direction according to the difference of the z coordinates of the surfaces between the B-scan and the reference image at the corresponding (x, y) position. We can also calculate the shift for each B-scan by means of the correlation coefficients between the corresponding A-lines in the circular and reference B-scans.

The blood vessels can be treated as straight lines in the small arc scan area. The Doppler angle can be calculated using the following relationship:

$$\cos \theta = \frac{\Delta z}{\sqrt{\Delta x^2 + \Delta y^2 + \Delta z^2}}, \quad (5)$$

Where  $\Delta x$ ,  $\Delta y$ , and  $\Delta z$  are the projections of the vessel segment in the scanned area on the X, Y, and Z axes. By differentiation of Eq. (5) we have

$$d(\cos \theta) = \frac{-\Delta x \Delta z d(\Delta x) - \Delta y \Delta z d(\Delta y) + (\Delta x^2 + \Delta y^2) d(\Delta z)}{(\Delta x^2 + \Delta y^2 + \Delta z^2)^{3/2}}. \quad (6)$$

In retina imaging,  $\theta$  is close to  $90^\circ$  and  $\Delta z \ll \Delta x, \Delta y$ . As a result, we can see from Eq. (6) the variation of the Doppler angle is more sensitive to the variation of  $\Delta z$ . So that compensation for eye movement in the z direction is the most important in calculating the Doppler angle.

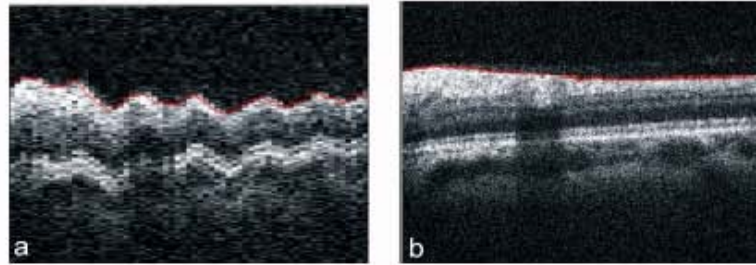


Fig. 2. (a). virtual B-scan extracted from the 3D data at the location of the reference scan. The red line shows the segmented ILM (inner limiting membrane) that is used for alignment. (b) The reference scan image.

Fig. 2 shows the extracted image (virtual B-scan) from the acquired 3D data corresponding to the positions of the linear reference scan together with the reference scan image. The inner limiting membrane (ILM) can be extracted by using our segmentation algorithm for both images. By comparing the Z coordinates at the same locations of the segmented ILM in both images, a compensation curve can be generated.



## 2.4 Automatic quantitative blood vessel detection

### 2.4.1 Automatic detection of lateral coordinates

To calculate the Doppler angle, the coordinates of the blood vessel need to be determined on each OCT cross sectional image. Our strategy is to first determine the lateral position and the diameter of each blood vessel on the cross sectional OCT intensity image and then determine the depth location of the vessel on the ODT image. In an OCT cross sectional image a blood vessel casts a shadow behind it, which exhibits as a low reflection region in the retinal fundus reflection graph. However, surface reflections can cause distortions to the blood vessel profile and add difficulty in blood vessel automatic detection. Other techniques were introduced to minimize the effect of surface reflection in retinal blood vessel detection. [12] Here we used our previously published method known as the shadowgram [11] to improve the retinal blood vessel profile and minimize the surface reflection effect. Using this technique we can generate a high contrast retinal reflection distribution called shadowgraph, where each vessel was characterized as a low reflection region.

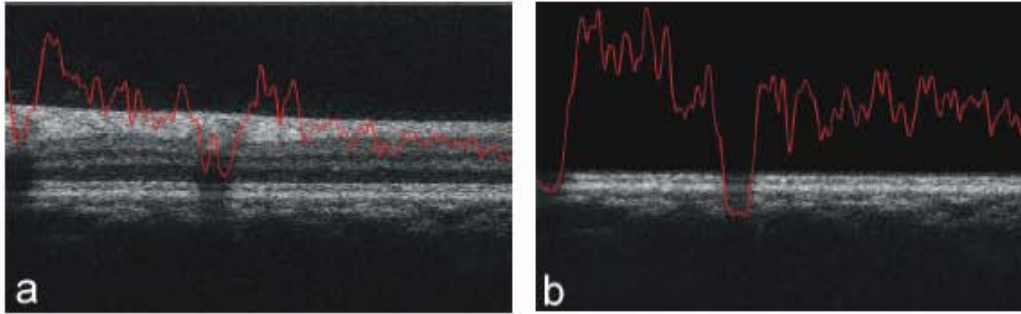


Fig. 3. Improved blood vessel profile using blood vessel shadowgraph. (a) Original B-scan image. (b) The B-scan image after the surface layer was removed. The calculated fundus reflection distribution corresponding to the B-scan and the fundus shadowgraph were superimposed on the images.

The shadowgraph was generated by first removing the surface layers of the retinal OCT image and then summing all the pixel intensity values along each A-scan. Fig. 3 shows the original OCT image, the image after the surface layer was removed, and the calculated reflection distributions (the vessel profiles). From the calculated fundus reflections we can see that not only the vessel contrast but also the vessel profile was improved by using the shadowgraph, which promises a more accurate detection of the vessel location and its diameter.

To extract the lateral coordinates the shadowgraph was first smoothed by using a smooth filter (Savitzky-Golay, length=3, weighing factor=21 in Matlab). The background was removed from the smoothed curve by subtracting the low pass filtered data. After normalization, thresholding according to a predetermined value was applied. The blood vessel locations and diameters were then determined.

### 2.4.2 Automatic detection of Depth coordinates

Automatically detecting the depth position of a blood vessel is much more challenging than detecting the lateral coordinates. Various methods may be used on either the intensity image or the ODT image. We first reported on the successful detection of the depth position of a blood vessel on an ODT image after the lateral coordinates and vessel diameter were determined. [6] The same method was used in the current study.

To detect the z coordinate of the center of a blood vessel, comprehensive information about the blood vessel was used, i.e. the lateral coordinates, the vessel diameter, and the Doppler shift caused by the blood flow. The basic idea is that outside the blood vessel the

calculated Doppler shift consists of only random noise where inside the vessel the Doppler shifts are correlated. Accordingly, a circular window filter moving in the z direction along the detected vessel position can be constructed. The diameter of the circular window should be equal or less than the diameter of the blood vessel. The filter can be either type of a function that examines the correlation of the values inside the window. The simplest type of the function is averaging.

We used an averaging filter for the detection of the z coordinate of a blood vessel. An average versus z curve was obtained for each blood vessel. A maximum or minimum will be reached, depending on the direction of the blood flow, when the center of the window coincides with the center of the blood vessel. Therefore, by locating the maximum or minimum of the average versus z curve the z coordinates of the center of a blood vessel can be determined.

Fig. 4 shows an example of the ODT image of a retinal blood vessel in an arc scan around the optic disc (a), the center of the blood vessel marked according to visual measurement (b), and the result of the moving circular window filtering. In this case, the location of the minimum corresponds to the center of the blood vessel. We can see from the figure that the moving circular window filtering worked well in locating the depth position of the vessel center.

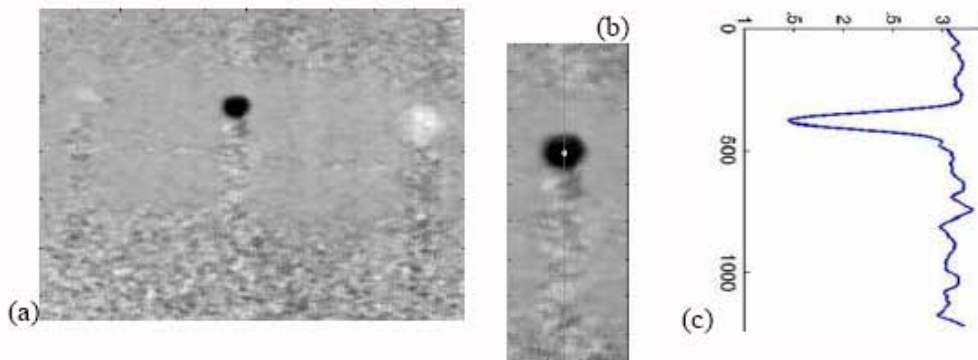


Fig. 4. Depth coordinate detection by using a circular window averaging. (a) The original ODT image of an arc scan; (b) The blood vessel center was marked by visual measurement; (c) Averaging curve along the direction of the A-line passing through the center of the blood vessel with a diameter of 60 pixels. Notice the position of the peak corresponds with the depth position of the center of the blood vessel.

Upon determination of the coordinates of a blood vessel the Doppler angle can be calculated by using Eq. (5). The absolute velocity of the blood flow inside the vessel can then be calculated. Knowing the absolute average velocity ( $\bar{v}_a$ , averaged across the vessel) of the blood flow and the vessel diameter (d), the blood flow rate (R) can be calculated as

$$R = \bar{v}_a \pi d^2 / 4. \quad (7)$$



Fig. 5 illustrates the procedure for the data processing.

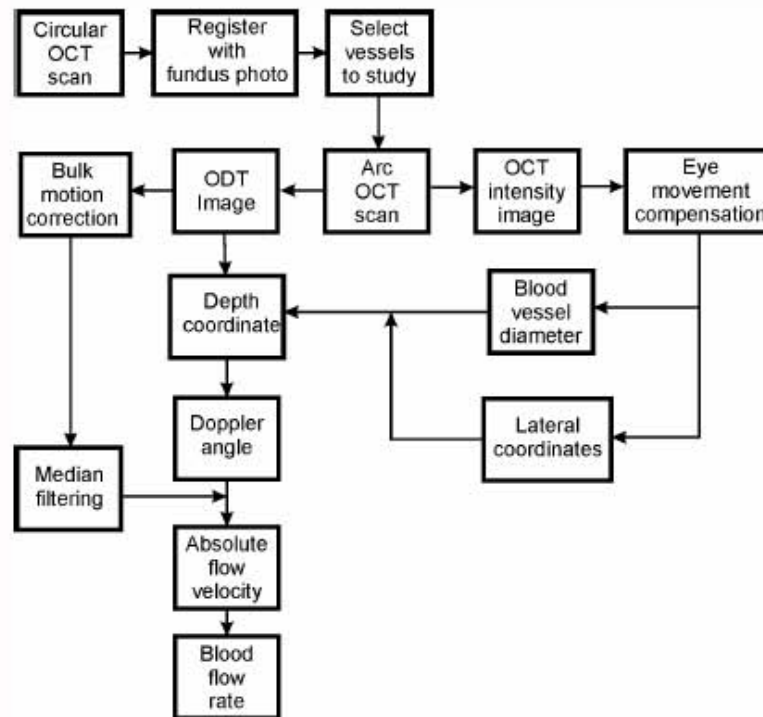


Fig. 5. Illustration of the procedure for calculation of the Doppler angle and the blood flow.

### 3. Results and discussion

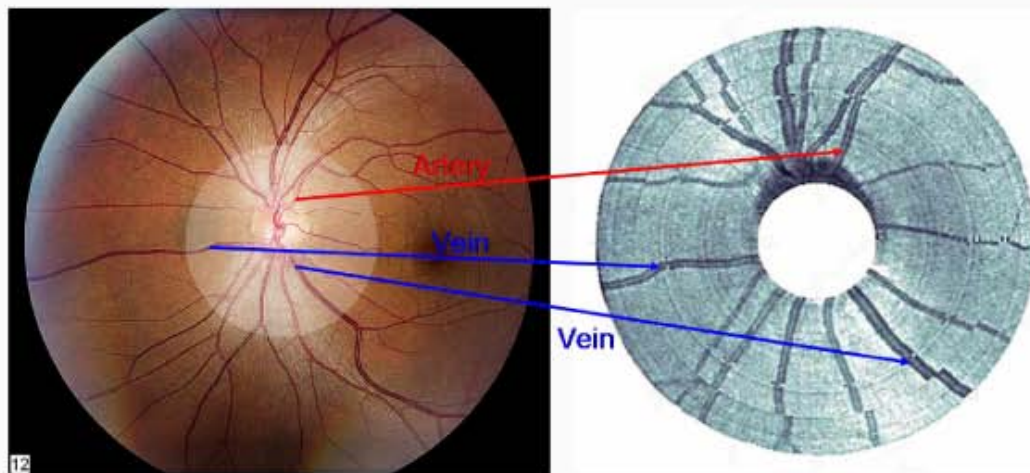


Fig. 6. Color fundus photograph of a normal human eye and the corresponding OCT fundus image generated from the circular scans around the optic disc.

The algorithms for detecting the vessel coordinates and diameters were applied to the measured data. Fig. 6 shows the re-constructed OCT fundus image from the circular scan around the optic disc and the corresponding color fundus photograph of a normal eye of a volunteer. By comparing both images retinal arteries and veins can be recognized on the OCT

fundus image. The OCT fundus image was used to determine the accuracy of the algorithm for the detection of the lateral position of the blood vessels. The OCT fundus image registered well with the fundus photograph. Fig. 7 shows the step-by-step data processing results and the detected vessel centers and vessel boundaries on the circular OCT and the ODT images.

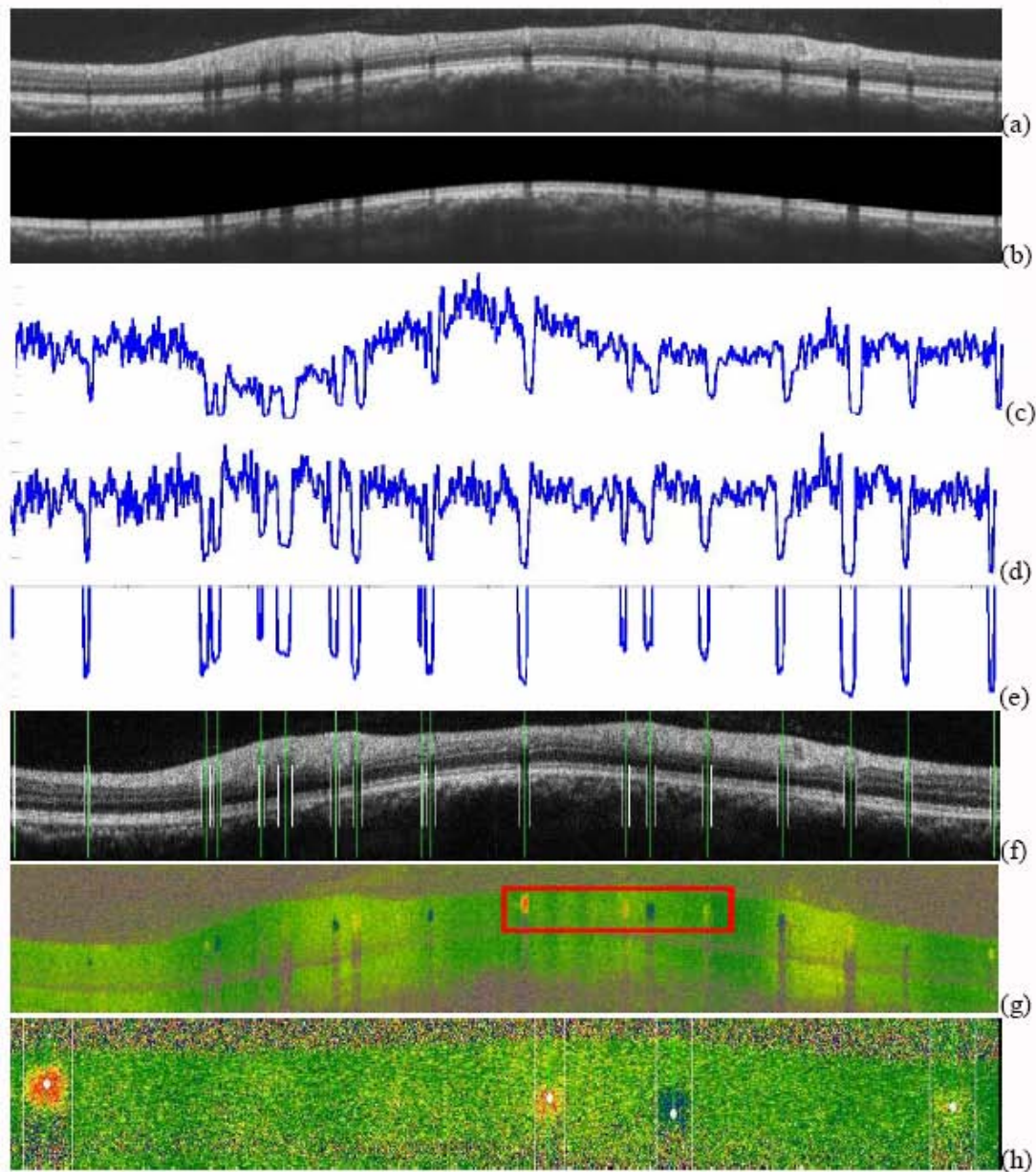


Fig. 7. (a). OCT image of a high density circular scan (8192 A-lines) around the optic disc of a normal human eye; (b). The OCT image after removal of the surface layers; (c). The original shadowgraph; (d). The shadowgraph after background correction and normalization; (e). the shadowgraph after thresholding; (f). Recognized blood vessel centers and boundaries are marked on the OCT image; (g). The ODT image for the same OCT scan; (h). Magnified view of the region marked in (g). where the calculated blood vessel centers are marked.

To test the accuracy of the algorithm the eyes of four normal volunteers were imaged and analyzed. We define the accuracy for the detection of the lateral coordinates as the percentage of the number of blood vessels automatically detected to the number of blood vessels detected



visually on the circular OCT fundus image. We achieved 100% accuracy for the eyes we have imaged. The accuracy for the detection of the depth coordinate was defined by comparing the visually determined blood vessel center on the Doppler image with the center determined by the algorithm (see Fig. 8 as an example). If the distance between the two centers was less than half of the radius of the vessel, we define it as a success. For the imaged normal eyes we achieved an accuracy of 84.4% for all the vessels. For large blood vessels (diameter larger than 50 pixels) depth positions were detected with an accuracy of 93.3%.

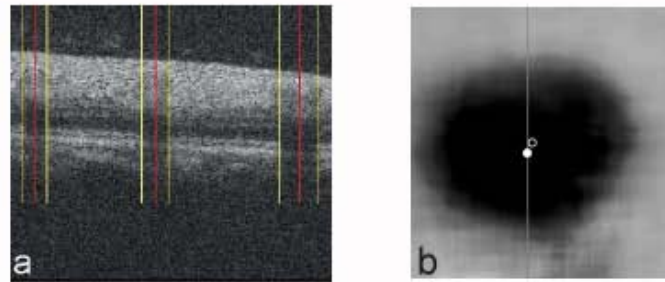


Fig. 8. (a). the detected vessel location and boundaries in an arc scan image; (b) comparing the automatically detected vessel center (solid circle) and the visually detected center (open circle) on the ODT image of a vessel.

The detected blood vessel coordinates contain the effect of eye movement. Before the vessel coordinates were used for calculation of the Doppler angle eye movement compensation was applied to the arc scans. After eye movement compensation linear fitting was used for the x, y, and z coordinates of the blood vessels. The angle of the fitted line in reference to the Z axis is the calculated Doppler angle. Fig. 9 shows the process and results for eye movement compensation for a blood vessel.

After calculation of the Doppler angle, the absolute blood flow velocity can be calculated. After the ODT image was median filtered the flow speed inside the blood vessel was averaged across the vessel for each time point to get the mean of the flow speed. One artery marked on Fig. 10(a) for a normal eye was studied. The calculated Doppler angle for this vessel is  $87.8^\circ$ . The calculated absolute velocity of the blood flow over time is shown in the curve of Fig. 10(b). The blood flow velocity over the time of measurement was calculated to be  $30.4 \pm 9.5$  mm/s (mean and standard deviation). The standard deviation reflects pulsating behavior of the artery. The volunteer's pulse rate measured separately immediately after the OCT imaging was 58 pulses/min, which agrees with the velocity calculation in Fig. 10b. The diameter of the vessel in the measured region is  $109 \mu\text{m}$ . As a result, the average blood flow in this vessel is  $17 \mu\text{l/min}$ .

One vein marked on the fundus photograph shown in Fig. 11(a) for another normal eye was also studied. The calculated Doppler angle for this vessel is  $87^\circ$ . The calculated absolute flow velocity of the blood flow, averaged across the vessel, is shown in the in Fig. 11(b). The averaged blood flow velocity over the time of measurement was calculated to be  $16.4 \pm 3.9$  mm/s (mean and standard deviation). The diameter of the vessel in the measured region is  $51 \mu\text{m}$ . As a result, the average blood flow in this vessel is  $2.01 \mu\text{l/min}$ .



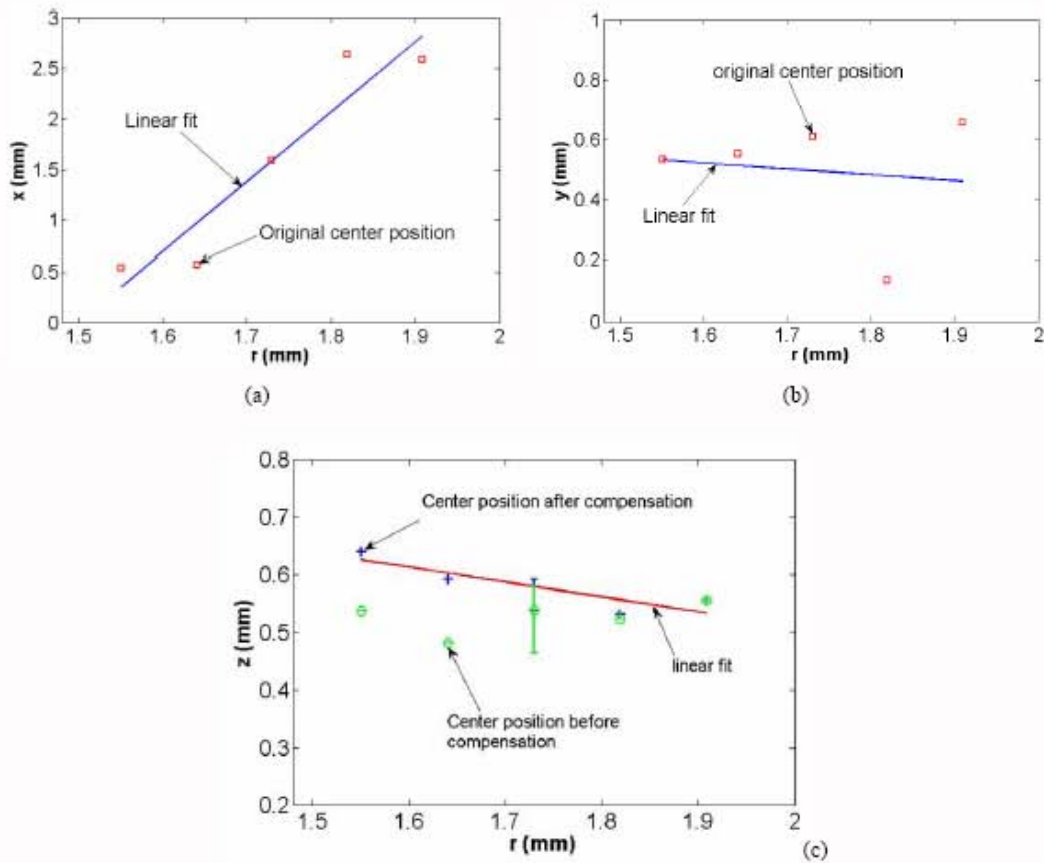


Fig. 9. The detected x, y, and z coordinates of the center of a blood vessel versus the scan radius  $r$ . Linear fitting were used for compensating variations of the x and y coordinates. The coordinates at  $r=1.73$  mm are the average of the results of the 58 repeated arc scans. (a) x versus  $r$ ; (b) y versus  $r$ ; (c) z versus  $r$  before and after eye movement compensation. Also shown in (c) is the range of the z coordinates of the vessel center for the 58 repeated arc scans.

ODT images for the artery and vein are also shown in Fig. 10 and Fig. 11. During the alignment for imaging acquisition a real-time ODT image was displayed for the position at the repeated arc scan. The ODT image for the blood vessel of interest was optimized by adjusting the optical head of the OCT system, which is equivalent to adjusting the Doppler angle for the specific vessel. When the ODT image for one vessel was optimized the quality of the images for the other vessels also covered by the scan may be deteriorated. We speculate the reason for this deterioration is caused by that the Doppler angle was closer to  $90^\circ$ .

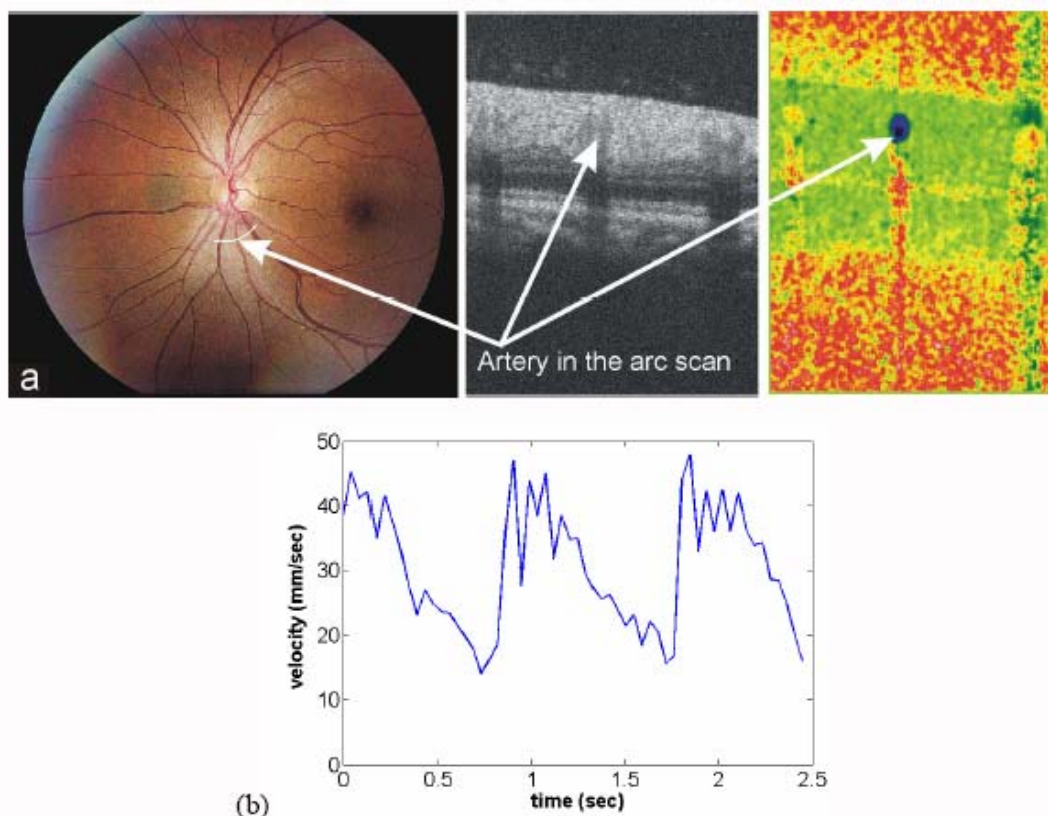


Fig. 10 The test result of an artery for a normal human eye. (a) The fundus photograph, the cross sectional OCT image at the position marked on the fundus photograph, and the ODT image. (b) The calculated absolute flow velocity averaged across the vessel area.

The calculated absolute velocity and flow rates for the artery and vein compared well with results obtained using other technologies.[13] The tests of the technique on current limited number of eyes were successful although more experiments are needed to test the accuracy and repeatability. Because the Doppler angles of retinal blood vessels are close to  $90^\circ$ , the error of the calculated absolute blood flow velocity is very sensitive to the error of the calculated Doppler angle. As analyzed in section 2.3 the Doppler angle is more sensitive to the eye movement in Z direction than that in X and Y directions, which is important considering that there is also no effective technique in the compensation for the movements in the X and Y directions. As a result, in our current technique eye movements in the X and Y directions were corrected only with linear fitting.

To test the accuracy of the calculation of the Doppler angle and the blood flow rate we measured the total flow rate of a vein before and after a bifurcation. Two measurements at the locations shown in Fig. 12 were taken. For the first measurement we scanned the area that contained the vein before bifurcation (parent vessel), while in the second measurement we scanned the area that contained both branches after bifurcation (daughter vessels). The time interval between the two measurements was about 15 minutes, during which the subject kept the same body position. The two measurements were taken at the same conditions where the room was kept dark to minimize the outside influence to the blood flow. The results of the measurements are shown in Table 1. The calculated average blood flow entering the bifurcation from the two branches was  $2.23 \mu\text{l}/\text{min}$  while the average blood flow leaving the bifurcation was  $2.17 \mu\text{l}/\text{min}$ . The result provided good validation of our technique for the calculation of the Doppler angle and the blood flow rate. We are planning to build a phantom



simulating a blood vessel with adjustable 3D orientation and flow rate to further test the accuracy of our algorithm.

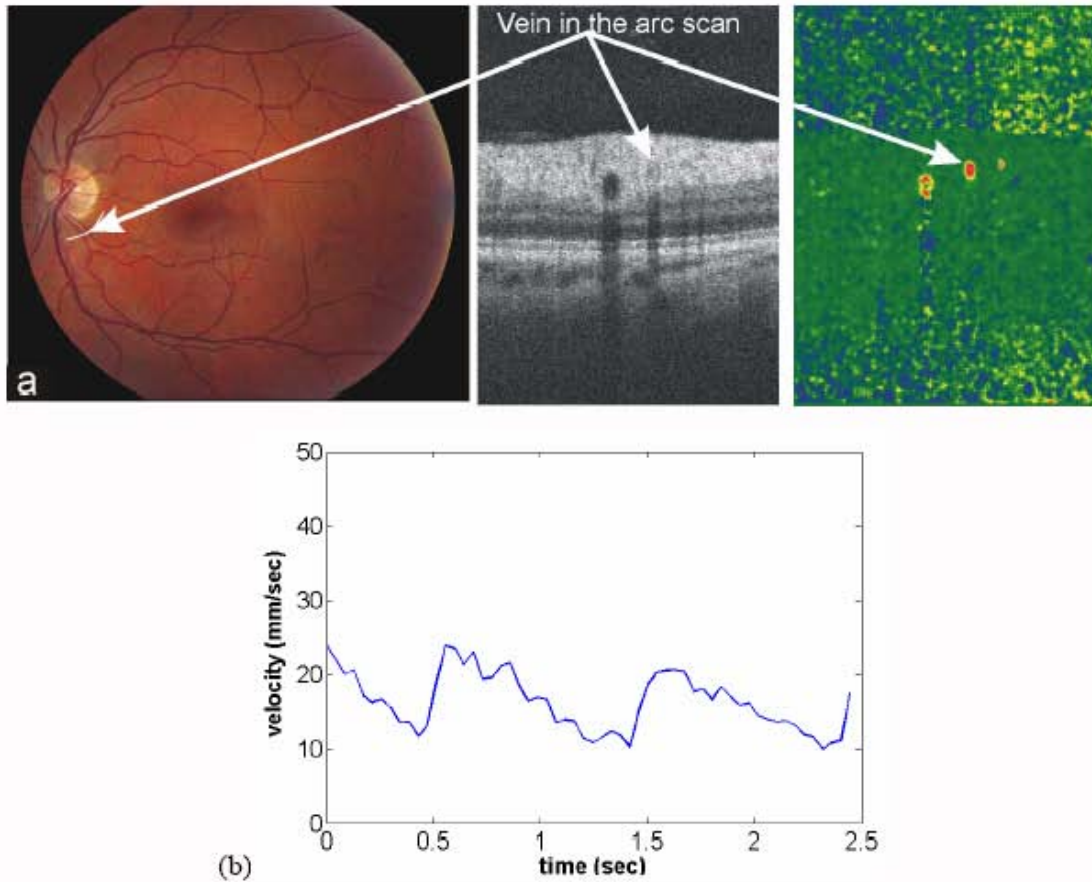


Fig. 11. The test result of a vein for a normal human eye. (a) The fundus photograph, the OCT cross sectional image at the position marked on the fundus photograph, and the ODT image. (b) The calculated absolute flow velocity averaged across the vessel area.

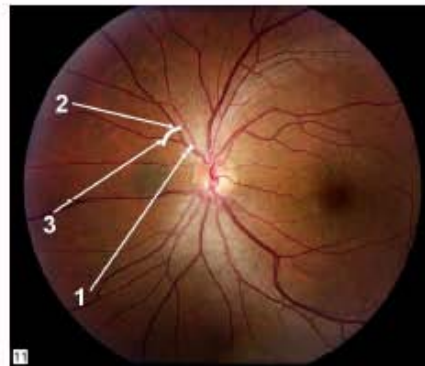


Fig. 12. Color fundus photograph of a normal human eye with markers indicating the location of the scan areas. Vessel 1 corresponds to the vein before bifurcation, while vessels 2 and 3 represent the vessel branches after bifurcation.

Table 1. Calculated parameters of the vessels shown in Fig. 12.

Vessel #	1	2	3
Diameter ( $\mu\text{m}$ )	103	66	54
Velocity (mm/sec)	4.3	8	4.12
Doppler Angle	81.6°	83°	76.3°
Flow ( $\mu\text{l}/\text{min}$ )	2.17 $\pm$ 0.57	1.65 $\pm$ 0.23	0.58 $\pm$ 0.07

#### 4. Conclusion

Doppler angle of retinal blood vessels including arteries and veins were successfully calculated by using the comprehensive information provided by high speed SD-OCT—structural information from the OCT intensity image and speed information from the ODT image. The lateral coordinates of a blood vessel can be extracted accurately by using the technique of blood vessel shadowgram, which not only enhanced contrast of the blood vessel against the reflecting background but also improved the vessels profile. The depth coordinate of a blood vessel was calculated by using a moving circular window filter in the ODT image after the lateral coordinates and the vessel diameter were extracted. By calculating the Doppler angle of a blood vessel the absolute blood flow velocity and the blood flow rate and be calculated. The technique was successfully tested on retinal arteries and veins for normal human eyes.

#### Acknowledgments

The authors thank Robert Knighton and Xiangrun Huang from Bascom Palmer Eye Institute University of Miami Miller School of Medicine for their support. This study is supported in part by the NEI P30 Core Grant Ey014801 and U.S. Army Medical Research and Materiel Command (USAMRMC) grant W81XWH-07-1-0188.